Paleogeothermal Gradients across an Inverted Hyperextended Rift System: Example of the Mauléon Fossil Rift (Western Pyrenees)

Nicolas Saspiturry, Abdeltif Lahfid, Thierry Baudin, Laurent Guillou-Frottier, Ph. Razin, Benoit Issautier, Benjamin Le Bayon, Olivier Serrano, Yves Lagabrielle, Benjamin Corre

Tectonics

RESEARCH ARTICLE
10.1029/2020TC006206

Key Points:
- We mapped paleogeothermal gradients in the Mauléon hyperextended rift from Raman spectroscopy of carbonaceous material in 155 samples
- The paleogeothermal gradient increases from cratonal values of 30°C/km in the proximal margin to 60°C/km in the hyperextended domain
- Inherited Early Cretaceous rift structure controlled the post collisional thermal history of the Mauléon basin

Supporting Information:
- Supporting Information S1
- Data Set S1

Correspondence to:
N. Saspiturry,
saspiturry.nicolas@gmail.com

Citation:
Saspiturry, N., Lahfid, A., Baudin, T., Guillou-Frottier, L., Razin, P., Issautier, B., et al. (2020). Paleogeothermal gradients across an inverted hyperextended rift system: Example of the Mauléon fossil rift (Western Pyrenees). *Tectonics*, *39*, e2020TC006206. https://doi.org/10.1029/2020TC006206

Received 19 MAR 2020
Accepted 12 AUG 2020
Accepted article online 17 AUG 2020

Paleogeothermal Gradients Across an Inverted Hyperextended Rift System: Example of the Mauléon Fossil Rift (Western Pyrenees)

N. Saspiturry[1], A. Lahfid[2], T. Baudin[2], L. Guillou-Frottier[2,3], P. Razin[1], B. Issautier[2], B. Le Bayon[2], O. Serrano[2], Y. Lagabrielle[4], and B. Corre[4]

[1]Université Bordeaux Montaigne/EA 4592 Géoressources & Environnement, Pessac, France, [2]Bureau de recherches géologiques et minières (BRGM), Orléans, France, [3]Institut des Sciences de la Terre d'Orléans, UMR 7327 Université d'Orléans, Centre national de la recherche scientifique (CNRS), Orléans, France, [4]Université Rennes, CNRS, Géosciences Rennes—UMR 6118, Rennes, France

Abstract The fossil rift in the North Pyrenean Zone, which underwent high temperature-low pressure metamorphism and alkaline magmatism during Early Cretaceous hyperextension, was studied to explore the geothermal regime at the time of rifting. In this work, we combined Raman lab analysis and thermal numerical modelling to shed light on the distribution of geothermal gradients across the inverted hyperextended Mauléon rift basin during Albian and Cenomanian time, its period of active extension. Data were acquired from a set of 155 samples from densely spaced outcrops and boreholes, analyzed using Raman spectroscopy of carbonaceous material. The estimated paleogeothermal gradient is strongly related to the structural position along the Albian-Cenomanian rift, increasing along a proximal-distal margin transect from ~34°C/km in the European proximal margin to ~37–47°C/km in the two necking zones and 57–60°C/km in the hyperextended domain. This pattern of the paleogeothermal gradient induced a complex interaction between brittle and ductile deformation during crustal extension. A numerical model reproducing the thermal evolution of the North Pyrenees since 120 Ma suggests that mantle heat flow values may have reached 100 mW/m^2 during the rifting event. This model reveals that above the thermal pulse, the temperature gradient varied within a small range of 55 to 62°C/km, as inferred from RSCM peak temperatures. We demonstrate that the style of reactivation during subsequent convergence influenced the thermal structure of the inverted rift system.

1. Introduction

The processes responsible for hyperextension of the continental crust have been widely studied in the present-day Atlantic conjugate margins based on interpretation of borehole data and petroleum seismic reflection profiles, for example, in central Norway and East Greenland (Kodaira et al., 1998; Mjelde et al., 2001, 2008; Peron-Pinvidic et al., 2012a, 2012b, 2013; Reston, 2007; Weigel et al., 1995), in Iberia and Newfoundland (Boillot et al., 1987, 1989; Driscoll et al., 1995; Haupert et al., 2016; Manatschal et al., 2001; Pérez-Gussinyé, 2013; Péron-Pinvidic et al., 2007; Péron-Pinvidic & Manatschal, 2009; Reston, 2009), and in Angola and Brazil (Aslanian et al., 2009; Aslanian & Moulin, 2013; Contrucci et al., 2004; Karner et al., 2003; Karner & Gambôa, 2007; Moulin et al., 2005, 2010; Unternehr et al., 2010). These systems have been numerically modeled to reproduce the paleogeometry of the continental margins and the detachment faults responsible for crustal thinning (Bai et al., 2019; Brune et al., 2014, 2016; Huismans & Beaumont, 2003, 2008, 2011, 2014; Lavier & Manatschal, 2006). These studies have shown that the Atlantic passive margins are characterized by three domains that increase in continental crustal thickness toward the craton: the hyperextended rift domain (less than 10 km thick), the necking zone (10–25 km thick), and the proximal margin (~30 km thick) (e.g., Péron-Pinvidic et al., 2015). The paucity of in situ tectonic and stratigraphic data available from the Atlantic passive margins has led researchers to study fossil passive margins in the Alps to better constrain the tectonic, sedimentary, and structural evolution of these margin domains (Beltrando et al., 2014; Decarlis et al., 2015; Froitzheim & Manatschal, 1996; Lemoine et al., 1987; Manatschal et al., 2000, 2006, 2011; Manatschal & Nievergelt, 1997; Masini et al., 2011, 2013; Mohn et al., 2012). However, few studies have described the thermal structure of such hyperextended systems (Clerc, 2012; Clerc et al., 2015; Corre, 2017; Hart et al., 2017; Nirrengarten et al., 2019; Vacherat et al., 2014).

Recent works on the fossil passive margin of the North Pyrenean Zone have established that outcrops of subcontinental mantle identified there (Fabriès et al., 1991, 1998) are the result of hyperextension of the continental crust during the Albian-Cenomanian rifting stage (Clerc et al., 2014; Clerc & Lagabrielle, 2014; Corre et al., 2016; Grool et al., 2018; Jammes et al., 2009; Labaume & Teixell, 2020; Lagabrielle et al., 2010, 2020; Lagabrielle & Bodinier, 2008; Masini et al., 2014; Mouthereau et al., 2014; Saspiturry, 2019; Saspiturry, Razin, et al., 2019; Teixell et al., 2016; Tugend et al., 2015). In contrast to the fossil margins in the Alps, where the hyperextended rift and oceanic domains were lost to Cretaceous subduction (Handy et al., 2010; Rubatto et al., 1998; Stampfli et al., 1998), the prerift to postrift sediments preserved in the inverted Pyrenean rift margins retain the imprint of the synrift thermal regime. The North Pyrenean Zone is a privileged place to trace the thermal imprint of hyperextension from the proximal rift margins to the hyperextended domain. The high-temperature, low-pressure metamorphism recorded on the North Pyrenean Zone rift system is interpreted as the consequence of continental crustal thinning during Early Cretaceous time (Albarède & Michard-Vitrac, 1978a, 1978b; Choukroune & Mattauer, 1978; Clerc et al., 2015; Debroas, 1990; Golberg et al., 1986; Golberg & Leyreloup, 1990; Golberg & Maluski, 1988; Montigny et al., 1986; Ravier, 1957; Vielzeuf & Kornprobst, 1984).

The work reported in this paper, based on Raman spectroscopy of carbonaceous material (RSCM) on the prerift to postrift sediments of the Mauléon basin in the North Pyrenean Zone (Figure 1), integrated paleotemperature data from 102 borehole samples and 54 outcrop samples. All the major domains of the Mauléon rift system were sampled in order to (1) obtain RSCM peak temperatures on the precollisional sedimentary infill, (2) examine the paleogeothermal gradients related to hyperextension in the proximal margin, necking zone, and hyperextended domain of the rift, and (3) define the effect of rift inheritance on the post collisional thermal regime. The RSCM methodology was coupled with a numerical thermal model, allowing us to (1) validate the coherence of the paleogradient estimated by RSCM, (2) estimate at what date the maximum temperature was reached by a rock that underwent the series of tectonic events recorded in the Mauléon basin, (3) constrain the present-day mantle heat flow values beneath the basin, and (4) estimate the synrift mantle heat flow beneath the basin.

2. The Mauléon Basin

2.1. Tectono-Sedimentary Evolution

The Mauléon basin is characterized by prerift deposits composed of (1) an Upper Triassic shale, evaporite and ophite complex (Curnelle, 1983; Lucas, 1985) and (2) Jurassic carbonate platform limestones and marls developed in a relatively stable tectonic context (Lenoble, 1992) (Figure 2). The top of the Jurassic section is characterized by large-scale exposure of the Aquitaine-Pyrenean domain, which was responsible for the removal by erosion of the Jurassic carbonate platform top and the absence of Neocomian deposits (Combes et al., 1998) (Figure 2).

During the early Barremian, localized subsidence of the previously emerged domain favored the transgression of carbonate platform deposits that continued until the earliest Albian (e.g., Arnaud-Vanneau et al., 1979). The end of this period was marked locally by extensive halokinetic deformation, associated with the appearance of normal faults (~120 Ma; e.g., Canérot et al., 2005). The deposition of a thick, deep-marine conglomeratic sequence on the southern margin of the newly formed Mauléon basin marked the onset of Albian rifting in the basin, indicating uplift of the Axial Zone of the Pyrenees (e.g., Saspiturry, 2019; Souquet et al., 1985). In the basin axis, more distal turbidites of the Albian to lower Cenomanian Black Flysch group, time-equivalent to the Mendibelza Conglomerates on the southern margin, constitute the first stratigraphic unit of the North Pyrenean rift. Along the more gently dipping northern margin, coeval Albian shallow-marine carbonate deposits grade southward to more distal marl-dominated sedimentation (Serrano et al., 2006).

The Mauléon basin widened during the middle Cenomanian to middle Santonian postrift stage (Razin, 1989). In the basin axis, a thick carbonate turbiditic system was deposited, supplied by the European platform to the north. At the southern margin, the transgressive "Calcaires des Cañons" carbonate platform onlapped the previously emerged Paleozoic basement, currently exposed in the Axial Zone (e.g., Alhamawi, 1992) (Figure 2).

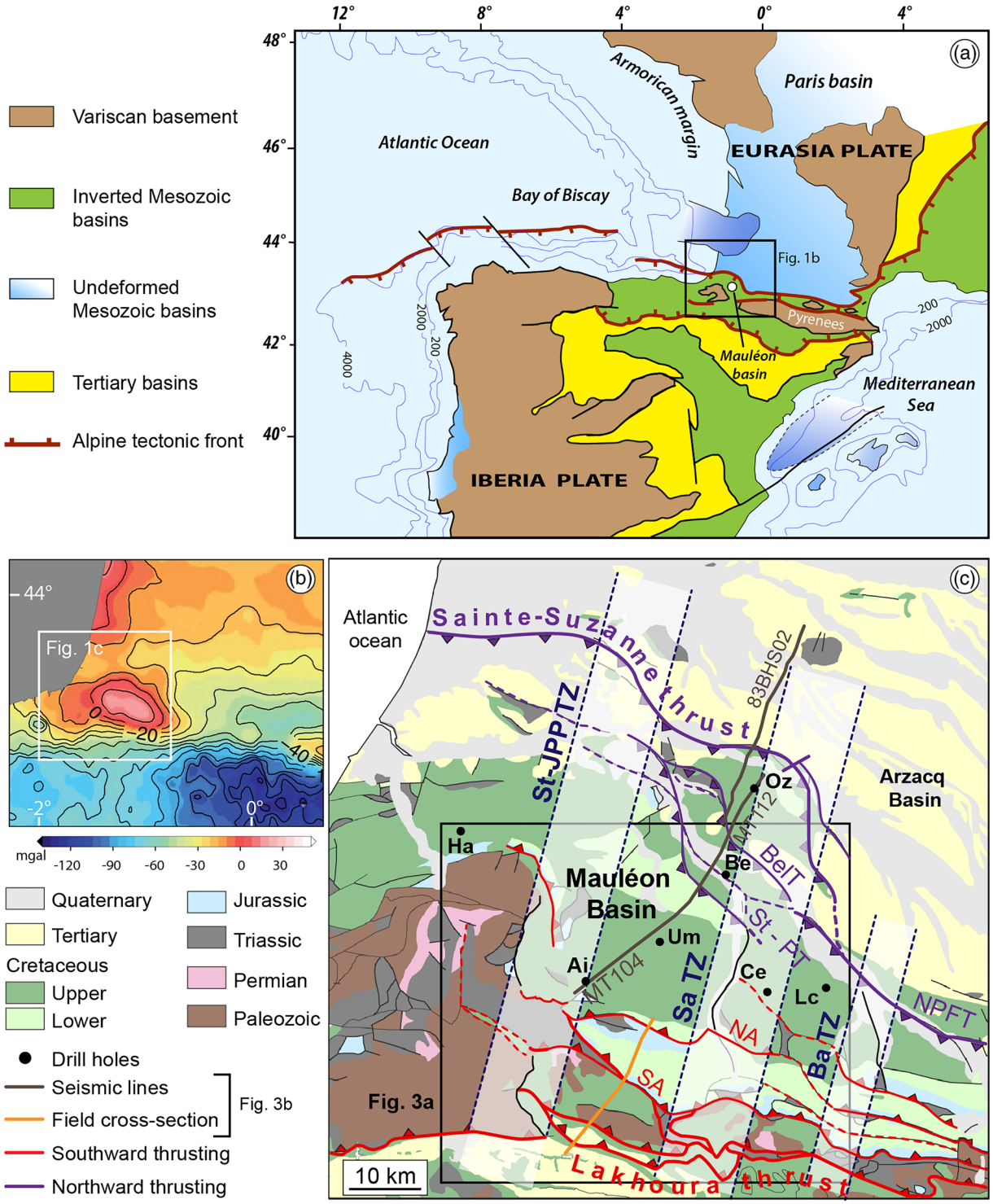

Figure 1. (a) Simplified structural map of the Cantabrian-Pyrenean orogenic system and adjoining Iberia showing deformed and undeformed domains in the Eurasia plate and the locations of basins in this study (modified from Lagabrielle et al., 2020). (b) Gravity anomaly map of the Pyrenees showing a positive Bouguer anomaly at the same location as the Mauléon basin (modified from Chevrot et al., 2018). (c) Geologic map highlighting the current pop-up structure of the Mauléon basin. The basin is offset by three transfer zones: St-JPP TZ, Saint-Jean-Pied-de-Port transfer zone; Sa TZ, Saison transfer zone; and Ba TZ, Barlanès transfer zone (Canérot, 2008, 2018a, 2018b; Debroas et al., 2010). Major thrusts include BelT, Bellevue thrust; NA, North Arbailles thrust; NPFT, North Pyrenean frontal thrust; SA, South Arbailles thrust; and St-PT, Saint-Palais thrust. Teeth are on the upthrown side; dashed where inferred. Drill holes are Ai, Ainhice-1; Be, Bellevue-1; Ce, Chéraute-1; Ha, Hasparren-101; Lc, Les Cassières-2; Oz, Orthez-102; and Um, Uhart-Mixe-1.

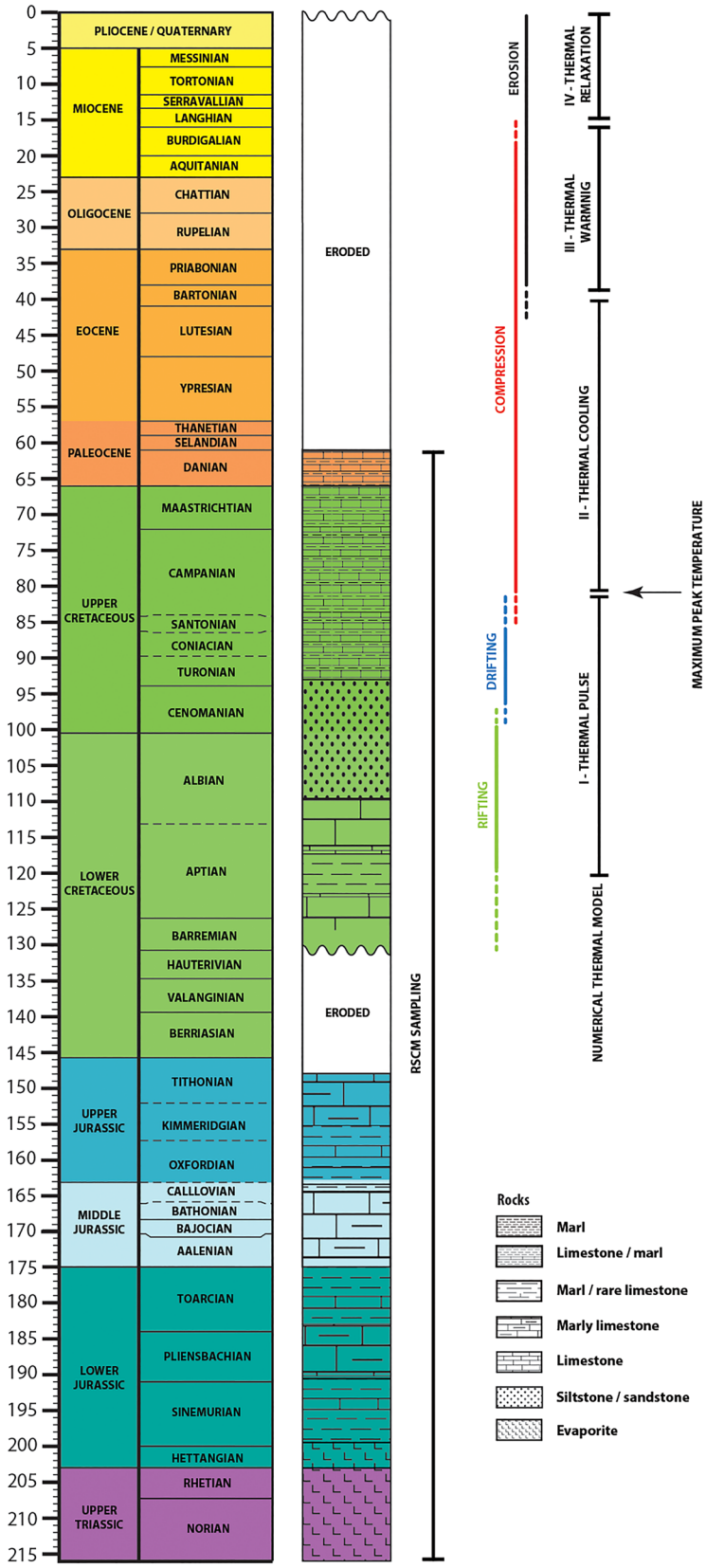

Figure 2. Stratigraphic diagram illustrating the Mauléon basin stratigraphic succession, the mean discontinuities, the RSCM samples locations, the geodynamic events, and the numerical simulation stages of Figures 10 and 11.

From late Santonian (~80 Ma) to middle Miocene time (~15 Ma), the Mauléon basin and the Aquitaine domain were affected by Pyrenean compression (Angrand et al., 2018; Labaume et al., 1985; Ortiz, 2019; Ortiz et al., 2019; Teixell, 1996, 1998; Vergés et al., 2002) responsible for the inversion of the Albian-Cenomanian hyperextended rift system (Garcia-Senz et al., 2019; Saspiturry, Allanic, et al., 2020; Teixell et al., 2016) and the deposition of a thick deep-water sequence derived from syntectonic siliciclastic systems to the east (Figure 2). This succession is no longer exposed in the Mauléon basin as the Pyrenean domain underwent exhumation and erosion starting in the Bartonian (~40 Ma; Bosch et al., 2016; Labaume et al., 2016; Vacherat et al., 2017). The Western Pyrenees ceased being affected by compression in the middle Miocene (15 Ma) during the postcollisional stage (e.g., Macchiavelli et al., 2017; Ortiz, 2019; Ortiz et al., 2019; Vergés et al., 2002).

2.2. Inverted Rift Domains

In the western Pyrenees, the North Pyrenean Zone corresponds to the inverted Mauléon basin (Figure 1; Ducasse & Vélasque, 1988; Souquet et al., 1977). The Mauléon basin is offset by the N20°E trending Saint-Jean-Pied-de-Port, Saison, and Barlanès transfer faults inherited from the Permian (Saspiturry, Cochelin, et al., 2019) and developed during the Albian rifting stage (Figure 1c; Canérot, 2008, 2018a, 2018b; Debroas et al., 2010). The Iberian (southern) proximal margin corresponds to the Axial Zone, consisting of a Paleozoic substratum overlain by a postrift Upper Cretaceous carbonate platform (Souquet, 1967), and the Paleozoic "Massifs Basques" (Muller & Roger, 1977) represent its western prolongation (Figure 3).

The Iberian necking zone, currently overthrusting the Axial Zone along the Lakhoura thrust (Teixell, 1993, 1998), is represented by the Mendibelza and Arbailles Units (Figures 3b and 3c). The Mendibelza Unit is composed of deep-sea Albian (synrift) and Upper Cretaceous (postrift) deposits overlying a Devonian to Permian substratum (Figure 3a; Boirie, 1981). The Arbailles Unit forms a syncline in which Paleozoic to Upper Triassic sediments are overlain by Jurassic (prerift) and Lower Cretaceous (synrift) carbonates and marls (Figure 3; Casteras et al., 1971; Lenoble, 1992).

The Mauléon basin hyperextended domain is bounded by the North Arbailles and the Saint-Palais reactivated synrift normal faults (Figure 3b; Saspiturry, Allanic, et al., 2020). This domain is composed of (1) a Jurassic to Lower Cretaceous carbonate cover displaced by gravity slides upon underlying evaporites of Triassic to Hettangian (earliest Jurassic) age (Bouquet, 1986; Corre et al., 2016; Ducasse et al., 1986; Lagabrielle et al., 2010), (2) Albian to lower Cenomanian (synrift) marls and fine-grained turbidites of the Black Flysch group (Fixari, 1984; Souquet et al., 1985), and (3) Upper Cretaceous (postrift) turbidites derived from the North Aquitaine carbonate platform on the European (northern) margin (Claude, 1990; Razin, 1989) (Figure 2).

The European margin is transported northward over the Arzacq basin on the Sainte-Suzanne thrust (Figure 3b; Angrand et al., 2018; Daignières et al., 1994; Issautier et al., 2020; Serrano et al., 2006; Teixell, 1998). Both sides involved are composed of a Jurassic to Albian carbonate platform and Upper Cretaceous turbidites.

3. The Cretaceous Pyrenean Metasomatic Event

3.1. High Temperature-Low Pressure Metamorphism

Synrift Pyrenean metamorphism is localized within the Internal Metamorphic Zone, a narrow east-west trending zone of metamorphosed and strongly deformed rocks (Casteras, 1933; Choukroune, 1974; Mattauer, 1968). The high temperature-low pressure metamorphism is characterized by a typical assemblage of muscovite, phlogopite, tremolite, plagioclase, potassium feldspar, and scapolite (Albarède & Michard-Vitrac, 1978a; Boulvais et al., 2006; Clerc et al., 2015; Golberg & Leyreloup, 1990; Golberg & Maluski, 1988; Montigny et al., 1986). The mineral assemblages indicate a maximum temperature of 550–650°C and a maximum pressure of 3–4 kbar (Bernus-Maury, 1984; Golberg & Leyreloup, 1990; Vauchez et al., 2013). Previous authors have established that this metamorphic event, which affected deposits of Triassic to Late Cretaceous age, featured a very high geothermal gradient resulting from continental crustal thinning (Dauteuil & Ricou, 1989; Golberg & Leyreloup, 1990). This event is also associated with deep-sea synrift sediments of the Black Flysch group (Debroas, 1978, 1987, 1990) and exposures of subcontinental mantle rocks (Clerc et al., 2012; Debroas et al., 2010).

Evidence for local denudation of the subcontinental mantle during the Early Cretaceous includes the presence of reworked clasts of mantle rocks in the late Albian to Cenomanian synrift sediments (Debroas

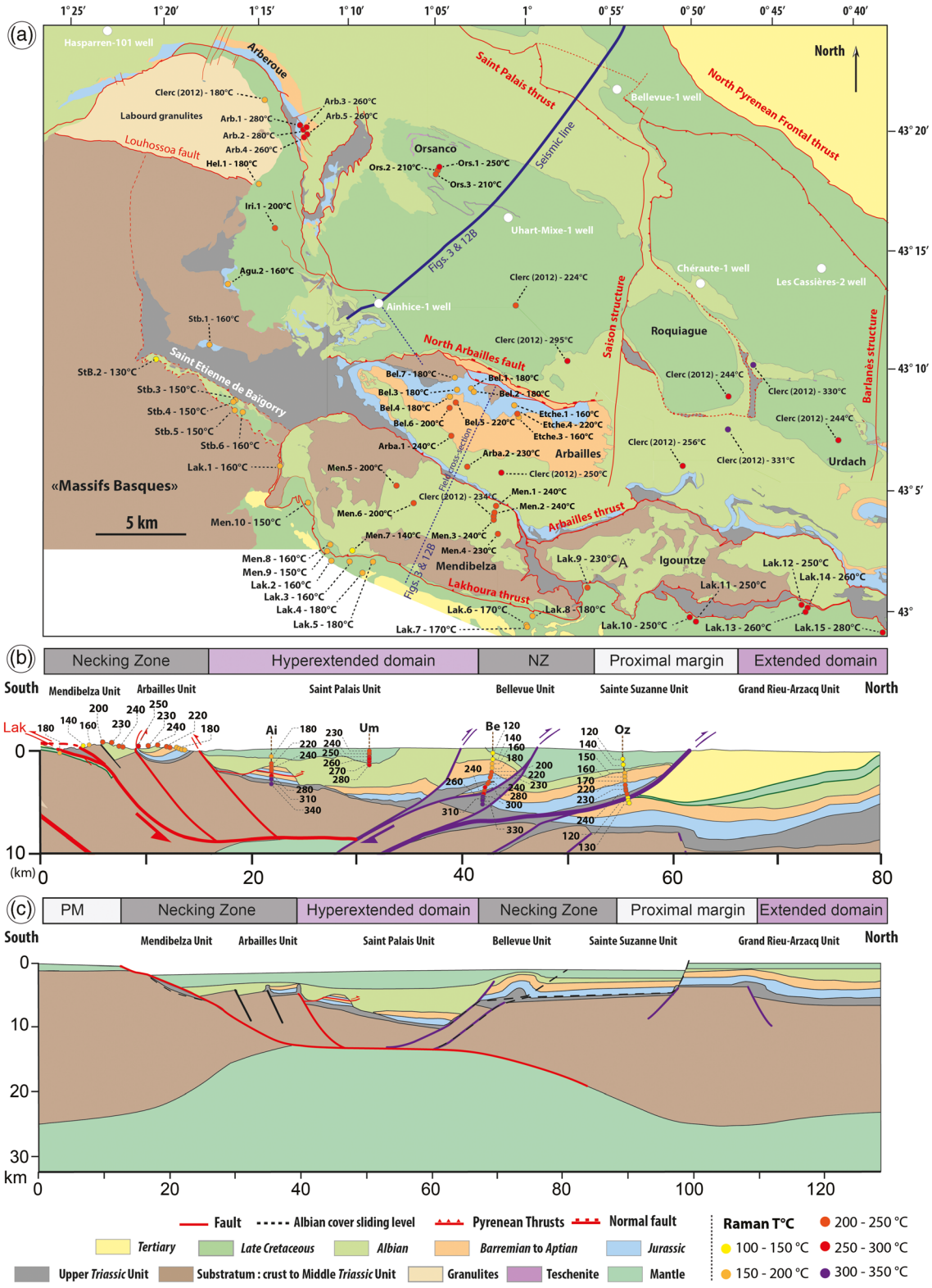

Figure 3. (a) Geologic map of the Mauléon basin showing locations of field samples and boreholes. Colors of field samples indicate their RSCM peak temperature. (b) N-S composite cross section of the Mauléon basin (Saspiturry, Allanic, et al., 2020) and RSCM peak temperatures (Raman T°C) in outcrop and borehole samples. (c) N-S Santonian palinspastic restoration of the Mauléon basin (Saspiturry, Allanic, et al., 2020). See Figure 1b for location. Major thrusts include Bel, Bellevue thrust; Lak, Lakhoura thrust; St-S, Sainte-Suzanne thrust; St-P, Saint-Palais thrust. Drill holes are Ai, Ainhice-1; Be, Bellevue-1; Oz, Orthez-102; Um, Uhart-Mixe-1; PM, Proximal Margin; and NZ, Necking Zone.

et al., 2010; Duée et al., 1984; Fortané et al., 1986; Jammes et al., 2009; Lagabrielle et al., 2010; Roux, 1983) and the association of a positive gravity anomaly with the Early Cretaceous North Pyrenean rift system (Figure 1b; Boillot et al., 1973; Casas et al., 1997; Chevrot et al., 2018; Daignières et al., 1994; Gottis, 1972; Grandjean, 1992, 1994; Wehr et al., 2018), interpreted as indicating the presence of subcontinental mantle at shallow depths (around 10 km) under the Mauléon basin (Figure 3b; Wang et al., 2016). Geochronological evidence indicates that mantle exhumation took place between 107 and 85 Ma (Albarède & Michard-Vitrac, 1978a; Golberg et al., 1986; Golberg & Maluski, 1988; Montigny et al., 1986; Thiébaut et al., 1992).

Recent studies based on RSCM have produced evidence that the Internal Metamorphic Zone reached temperatures ranging from 400°C to 600°C in the central and eastern Pyrenees (Chelalou et al., 2016; Clerc, 2012; Clerc et al., 2015; Ducoux, 2017; Lagabrielle et al., 2016) to 200–630°C in the Nappes des Marbres at its western end, southwest of the Mauléon basin (Ducoux, 2017; Lamare, 1936; Martínez-Torres, 1989; Mendia & Ibarguchi, 1991). Hydrothermal fluid circulation can account for the local thermal homogeneity in the Internal Metamorphic Zone, for instance, in the Boucheville basin in the eastern part of the North Pyrenean Zone, where the temperature range was 530–580°C (Boulvais, 2016).

3.2. Alkaline Magmatism, Albitization, and Talc Mineralization

The North Pyrenean Zone underwent widespread Mesozoic magmatic activity, attested by Cretaceous alkaline magmatism (Montigny et al., 1986; Rossy et al., 1992). The Cretaceous igneous rocks consist of alkaline basalt and trachyte, as well as intrusive teschenyte and syenite (Azambre et al., 1992; Azambre & Rossy, 1976; Thiébaut et al., 1979). The Cretaceous volcanism was predominantly submarine, characterized by pillow basalt and pyroclastic rocks. The position of these rocks within Cretaceous sedimentary deposits ensures reliable biostratigraphic ages for this magmatic event. They range in age from late Albian to Santonian in the western Pyrenees (Castañares et al., 1997; Casteras et al., 1970; Lamolda et al., 1983; López-Horgue et al., 1999; Rat, 1959; Rat et al., 1983; Schoeffler et al., 1964) and from late Albian to Turonian in the central Pyrenees (Debroas, 1990; Dubois & Seguin, 1978) and eastern Pyrenees (Montigny et al., 1986).

These biostratigraphically constrained ages are consistent with the radiometric dates available for the Cretaceous magmatic rocks, which range from 115 to 85 Ma (Golberg et al., 1986; Henry et al., 1998; Montigny et al., 1986). Some amphibolite, pyroxenite, and hornblende dikes in the North Pyrenean mantle rocks might be derived from alkaline magmatism (Bodinier et al., 1988, 2004). Radiometric ages of these rocks are similar to those of the alkaline magmatism: 116 $\pm$ 5 Ma (Verschure et al., 1967) and 101 $\pm$ 2.5 Ma (Golberg et al., 1986) in Lherz, 103 $\pm$ 2 Ma in Caussou (Albarède & Michard-Vitrac, 1978a), and 103 Ma in Urdach (Azambre & Monchoux, 1998).

The high temperature-low pressure metamorphism and alkaline magmatism affecting the North Pyrenean Zone were synchronous with the albitization of the Agly, Salvezine, Saint-Barthélémy, and Arize massifs in the North Pyrenean Zone (Boulvais et al., 2007; Poujol et al., 2010) and the formation of thick talc-bearing intervals (Moine et al., 1989), characterized by fluid temperatures ranging from 250°C to 550°C, during hydrothermal alteration that took place between 117 and 92 Ma (Boulvais et al., 2006; Fallourd et al., 2014).

4. Methods

4.1. RSCM Thermometry

Raman measurements were performed at BRGM using a Renishaw inVia Reflex microspectrometer with a diode-pumped solid-state laser source excitation of 514.5 nm. The laser power reaching the sample surface, through the 100X objective (numerical aperture 0.90) of a Leica DM2500 microscope, did not exceed 0.1 mW. Before each measurement session, the microspectrometer was calibrated using the 520.5 cm^{-1} line of an internal silicon standard. After Rayleigh diffusion was eliminated by edge filters, the Raman signal was first dispersed using 1,800 lines/mm signal before analysis with a deep depletion CCD detector (1,024 $\times$ 256 pixels). In certain contexts, such as areas of contact metamorphism, at least 25 spectra need to be acquired (Aoya et al., 2010). Lacking evidence of contact metamorphism, we applied the Lahfid et al. (2010) analytical protocol and acquired 10–15 spectra to ensure consistent data. Renishaw Wire 4.1 software was

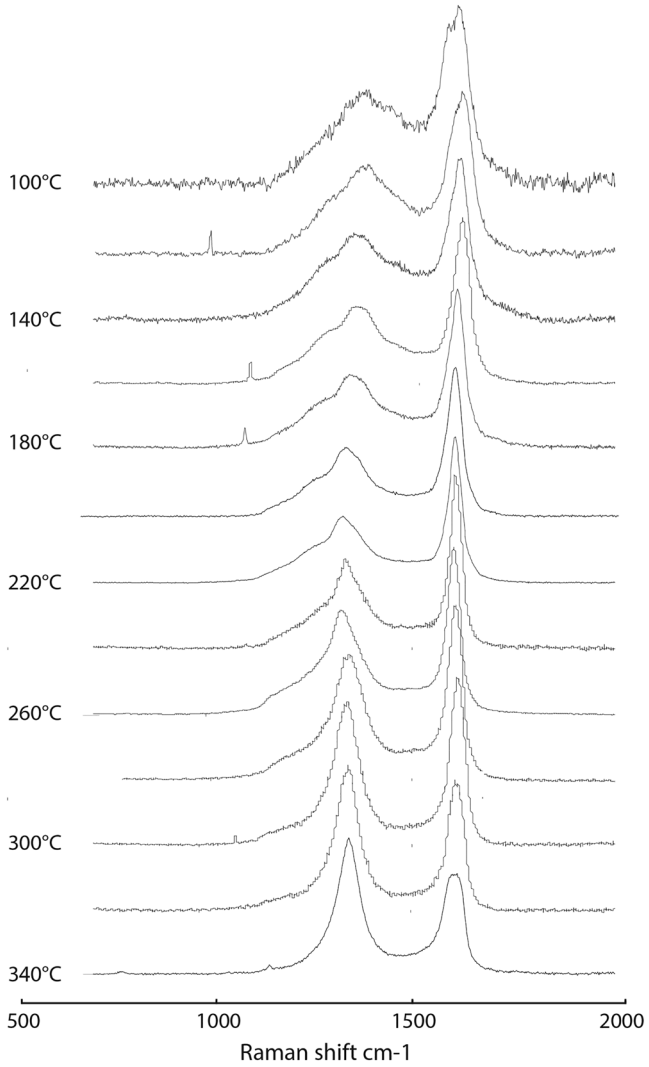

Figure 4. Representative Raman Spectra of carbonaceous materials corresponding to temperatures varying from 100°C to 340°C with a step of 20°C. These spectra were used in this work to attribute qualitative temperature of rocks.

used for instrument calibration and Raman measurements. More spectra were routinely acquired in samples that were observed to be highly heterogeneous.

The Raman spectrum of carbonaceous material is composed of first-order and second-order regions. In our study, we recorded Raman spectra only for the first-order region (700–2,000 cm^{-1}), where we mainly observed two wide bands: the defect band (D; centered at ~1,350 cm^{-1}) and the graphitic band (G; centered at ~1,580 cm^{-1}) (see Henry et al., 2019, for a review). The Raman spectrum of pristine graphite displays only the G band; for less ordered structures of graphite the defect bands D1 (~1,350 cm^{-1}) and D2 (~1,620 cm^{-1}) also appear (e.g., Beyssac et al., 2002). Other bands are seen in Raman spectra for disordered structures of carbonaceous material that has experienced maximum temperatures of 200–350°C (e.g., Lahfid et al., 2010; Sadezky et al., 2005) such as D3 (~1,500 cm^{-1}) and D4 (~1,250 cm^{-1}). More strongly disordered structures of carbonaceous material display additional bands at 1,150 and 1,400 cm^{-1} (Ferralis et al., 2016; Rebelo et al., 2016; Schito et al., 2017).

The continuous evolution from disordered to ordered structure in carbonaceous material is mainly dependent on temperature and thus can be used as an indicator of the diagenetic or metamorphic grade of rocks. This evolutionary process can be measured using Raman microspectroscopy (e.g., Guedes et al., 2010; Jehlička et al., 2003; Marques et al., 2009; Wopenka & Pasteris, 1993; Yui et al., 1996). A geothermometer based on RSCM has been calibrated, initially for the temperature range of 330–650°C, to calculate peak temperatures of regional metamorphism (Beyssac et al., 2002) or contact metamorphism (Aoya et al., 2010) and subsequently extended to 200–330°C, temperatures typical of diagenesis and low-grade metamorphism (e.g., Lahfid et al., 2010). More recent work has extended the applicability of RSCM to temperatures lower than 200°C (Henry et al., 2018, 2019; Hinrichs et al., 2014; Lahfid et al., 2019; Lunsdorf et al., 2017; Schito & Corrado, 2018; Schmidt et al., 2017; Zhou et al., 2014), and Schito et al. (2017) has proposed a reference Raman spectrum for the range 80–200°C. These studies have highlighted several parameters that can serve as temperature indicators; however, the correlation curves between these parameters and vitrinite reflectance are significantly different. These differences may arise from the data treatment (the curve fitting procedure selected) or the analytical protocols followed.

In this study, we used a series of reference Raman spectra published by Lahfid et al. (2010) and Schito et al. (2017) for the range 100–340°C. We identified reference Raman spectra for carbonaceous material at 12 20°C steps in this temperature range (100, 120, 140, ..., 300, 320, and 340°C; Figure 4). The ±20°C error bars on the figures represent the absolute uncertainty of maximum temperatures attributed to Raman spectra in the range 100–340°C. This ±20°C error is applied equally to all RSCM peak temperature data rather than to individual samples. Our determinations of RSCM peak temperature were based on comparisons of the Raman spectrum shape of each sample to the reference series in Figure 4. Thus, in this study, all maximum temperatures determined by RSCM geothermometry are qualitative estimates.

4.2. Calculation of Paleogeothermal Gradients

The geotherm, defined as the temperature profile versus depth, can be linear in the crust and the lithosphere if the medium is uniform and internal heat production is negligible. Where the crust is heterogeneous, however, contrasts in thermal conductivity may perturb the geotherm from linearity. In addition, radiogenic heat production in crustal rocks results in a curved geotherm in which the geothermal gradient decreases with depth. Advective processes of various scales can also disturb the thermal regime of the crust.

Diapirism, magmatism, and hydrothermal fluid circulation can significantly affect the geotherm over periods ranging from several tens of thousands to millions of years, and tectonic events such as collision and thrusting, rifting (crustal extension), and coeval erosion or sedimentation lead to transient evolution of crustal temperatures at longer time scales (e.g., Jaupart & Mareschal, 2011; Magri et al., 2015; Nábělek & Nábělek, 2014).

In this study, we estimated paleogeothermal gradients across the Cretaceous extended precursor of the Mauléon basin, using RSCM peak temperatures measured in transects of surface rocks and in cuttings from deep petroleum wells. Because the investigated depths do not exceed 6,000 m, the relatively fixed temperature conditions at the surface force the geotherm to remain nearly linear. Using RSCM peak temperatures to estimate paleogeothermal gradients is not an easy task because rocks may theoretically record several peak temperatures over the course of geologic time. We ran a series of thermal models to test the sensitivity of the Mauléon basin to its particular tectonic history (see section 5) and found that the maximum peak temperatures recorded during Cretaceous time were the highest ones since 120 Ma. On that basis, we attempted to deconvolve the signal of the paleogeothermal gradient for each field section or well.

Of the seven boreholes used in this study, only the Ainhice-1 well was strictly vertical, thus the other six required adjustments for their deviations from vertical before evaluating their thermal gradients. The Chéraute-1 well had the largest deviation, amounting to 742 m at the bottom of the borehole. The other depth deviations were 313 m for Bellevue-1, 251 m for Les Cassières-2, 165 m for Hasparren-101, 88 m for Orthez-102, and 13 m for Uhart-Mixe-1. Linear regressions for all boreholes except the Chéraute-1 well are characterized by coefficient values of best fit (R^2) of 0.95 or greater, their slopes corresponding to the apparent thermal gradient. This gradient was then corrected for each borehole on the basis of the mean stratal dip to yield the paleogeothermal gradient that existed before inversion of the Mauléon basin. When crustal deformation occurred prior to the time the RSCM peak temperature was reached, the paleogeothermal and apparent thermal gradients are the same. Considering the ±20°C error of the RSCM peak temperature (see section 4.1), the linear regression line is shifted from ±20°C but its slope and intercept are unchanged. Thus, the paleogradient estimation is unaffected by this uncertainty.

We also had to consider the case where a segment of the paleogeotherm was vertical or nearly so. A homogeneous temperature profile over a substantial vertical depth may be caused by homogenization of temperatures due to hydrothermal convection (e.g., temperature profiles in geothermal systems; Guillou-Frottier et al., 2013), localized ascent or descent of hydrothermal fluids (e.g., upflow through permeable fault zones; Roche et al., 2018), or refraction effects due to bodies with high thermal conductivity, such as salt domes or evaporite layers (e.g., Guillou-Frottier et al., 2010; Magri et al., 2008; Mello et al., 1995). In this latter case, the geotherm is not truly vertical, but the temperature gradient can be decreased by a factor of 2 to 3. When temperature profiles describe such a decreased thermal gradient (DG), the paleogeothermal gradient cannot be evaluated, as was the case for the Hasparren-101 and Chéraute-1 wells.

5. Results

Representative RSCM peak temperature spectra are shown in Figure 5, for the field samples and for each of seven boreholes, and the resulting temperatures are listed in Table 1 for the field samples and in Table 2 for the borehole samples (Saspiturry, Lahfid, et al., 2020). Uncorrected and corrected borehole depths are reported as measured depth (MD) and true vertical depth (TVD), respectively, in Table 2. Columnar sections of the boreholes and field sites, annotated with these RSCM peak temperatures, are presented along a north-south transect in Figure 6 and an east-west transect in Figure 7. Figure 8 presents the RSCM peak temperatures measured in boreholes with respect to TVD, and Figure 9 illustrates the RSCM peak temperatures measured on the field sections. The linear regression lines drawn for the seven boreholes are characterized by R^2 values of 0.95 or greater, except in the case of the Chéraute-1 well.

5.1. Iberian Proximal Margin

Our paleogeothermal analysis of the Iberian proximal margin is based on 15 outcrop samples of Santonian to Danian age (syncollisional) exposed beneath the Lakhoura thrust in the Axial Zone just south of the Mendibelza Unit (Figures 3 and 6). These samples yielded RSCM peak temperatures ranging from 160°C to 180°C in the west to 280°C in the east (Figure 5a and Table 1). Because most of the samples were from

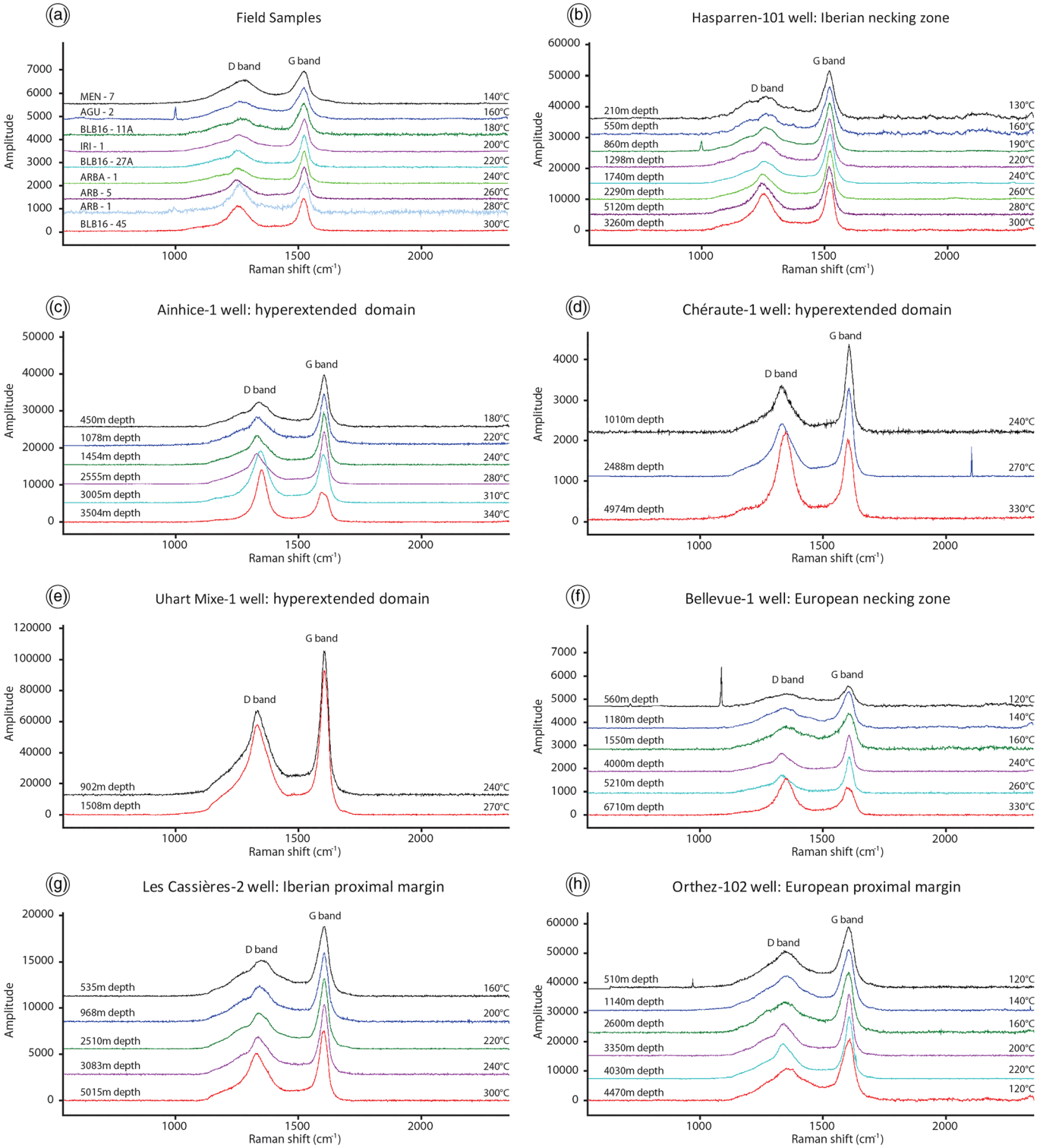

Figure 5. Representative Raman spectra of carbonaceous materials showing temperature increases in (a) outcrops, (b) Hasparren-101 well, (c) Ainhice-1 well, (d) Chéraute-1 well, (e) Uhart-Mixe-1 well, (f) Bellevue-1 well, (g) Les Cassières-2 well, and (h) Orthez-102 well. Curves are offset for visibility. See Figure 2a for wells and samples location.

Table 1
Description of Outcrop Samples; Locations Are in WGS84 Coordinates

Sample	Latitude	Longitude	Age	Lithology	Raman temperature (°C)
Axial Zone: Iberian Proximal Margin					
LAK-1	43.102108	−1.219360	Maastrichtian	Calcschist	160
LAK-2	43.036917	−1.177413	Danian	Calcschist	160
LAK-3	43.035055	−1.162842	Campanian	Calcschist	160
LAK-4	43.023748	−1.144220	Danian	Marl	180
LAK-5	43.034887	−1.135020	Campanian	Calcschist	180
LAK-6	42.991763	−0.986248	Campanian	Calcschist	170
LAK-7	42.991763	−0.986248	Campanian	Calcschist	170
LAK-8	42.998580	−0.985852	Campanian	Calcschist	180
LAK-9	43.018367	−0.937463	Campanian	Calcschist	230
LAK-10	42.999257	−0.838788	Campanian	Calcschist	250
LAK-11	42.994837	−0.834207	Campanian	Calcschist	250
LAK-12	43.005373	−0.731272	Campanian	Calcschist	250
LAK-13	43.002290	−0.725235	Campanian	Calcschist	260
LAK-14	43.003928	−0.724552	Campanian	Calcschist	260
LAK-15	42.996247	−0.684223	Campanian	Calcschist	280
Mendibelza Unit: Iberian Necking Zone					
MEN-1	43.071898	−1.019520	Early Albian	Siltstone	240
MEN-2	43.069752	−1.021996	Early Albian	Siltstone	240
MEN-3	43.065726	−1.023290	Early Albian	Siltstone	240
MEN-4	43.053575	−1.017703	Early Albian	Siltstone	230
MEN-5	43.089358	−1.111091	Middle Albian	Siltstone	200
MEN-6	43.080316	−1.098856	Middle Albian	Siltstone	200
MEN-7	43.042209	−1.151609	Late Albian	Siltstone	140
MEN-8	43.040542	−1.172827	Santonian	Breccias	160
MEN-9	43.040623	−1.172787	Coniacian	Siltstone	150
MEN-10	43.069492	−1.194545	Santonian	Breccias	150
Saint-Etienne-de-Baïgorry Unit: Iberian Necking Zone					
STB-1	43.181566	−1.284771	Early Jurassic	Limestone	160
STB-2	43.170830	−1.336082	Late Albian	Marls	130
STB-3	43.136767	−1.264075	Santonian	Calcschist	150
STB-4	43.141252	−1.261580	Santonian	Calcschist	150
STB-5	43.140792	−1.261903	Santonian	Calcschist	150
STB-6	43.137648	−1.257442	Santonian	Calcschist	160
Arbailles Unit: Iberian Necking Zone					
BEL-1	43.151402	−1.042786	Early Jurassic	Marly limestone	180
BEL-2	43.152268	−1.045087	Middle Jurassic	Marly limestone	180
BEL-3	43.149475	−1.055378	Late Jurassic	Marly limestone	180
BEL-4	43.147340	−1.059262	Barremian	Marl	180
BEL-5	43.144710	−1.058376	Aptian	Marl	220
BEL-6	43.141317	−1.065354	Aptian	Limestone	200
BEL-7	43.157929	−1.053770	Early Jurassic	Marly limestone	180
ETCH-1	43.138797	−1.003380	Middle Jurassic	Marly limestone	160
ETCH-3	43.135267	−0.998984	Aptian	Limestone	160
ETCH-4	43.135725	−0.999518	Aptian	Limestone	220
ARBA-1	43.100010	−1.051226	Earliest Albian	Marl	240
ARBA-2	43.121969	−1.063731	Earliest Albian	Marl	230
Arberoue Unit: Iberian Necking Zone					
ARB-1	43.332444	−1.200691	Late Jurassic	Marly limestone	280
ARB-2	43.331583	−1.199066	Late Jurassic	Marly limestone	280
ARB-3	43.331834	−1.198787	Barremian	Limestone	260
ARB-4	43.329313	−1.198841	Barremian	Limestone	260
ARB-5	43.327623	−1.197450	Aptian	Marl	260
Hyperextended Domain					
ORS-1	43.300258	−1.075456	Turonian	Marl	250
ORS-2	43.301730	−1.074582	Turonian	Marl	210
ORS-3	43.302269	−1.074059	Turonian	Marl	210
IRI-1	43.257235	−1.232790	Santonian	Calcschist	200
AGU-2	43.222597	−1.271063	Late Jurassic	Limestone	160
HEL-1	43.293563	−1.240483	Santonian	Calcschist	180

Table 2
Description of Well Samples

Measured depth (m)	True vertical depth (m)	Age	Lithology	Raman temperature (°C)
Hasparren-101 Well: Iberian Necking Zone				
210	210	Early Cenomanian	Marl	130
420	420	Early Cenomanian	Marl	140
550	550	Early Cenomanian	Marl	160
700	700	Early Cenomanian	Marl	170
860	860	Early Cenomanian	Marl	190
1,060	1,060	Early Cenomanian	Marl	200
1,298	1,298	Early Cenomanian	Marl	220
1,500	1,500	Early Cenomanian	Marl	230
1,740	1,740	Early Cenomanian	Marl	240
2,040	2,040	Early Cenomanian	Marl	250
2,290	2,290	Early Cenomanian	Marl	260
2,790	2,790	Early Cenomanian	Marl	240/280
3,120	3,120	Albian	Marl	280
3,260	3,260	Late Jurassic	Marl	300
3,410	3,410	Late Jurassic	Marl	280
3,680	3,680	Early Jurassic	Limestone	270
4,120	4,117	Early Jurassic	Clay	280
4,390	4,387	Late Triassic	Clay	280
4,760	4,757	Late Triassic	Clay	240/280
5,120	5,117	Late Triassic	Clay	280
5,550	5,543	Turonian	Calcschist	240
5,870	5,827	Turonian	Calcschist	220
6,050	5,960	Turonian	Calcschist	220
6,220	6,055	Permian	Clay	240
6,270	6,105	Permian	Clay	240
6,280	6,115	Paleozoic	Clay	230
Ainhice-1 Well: Hyperextended Domain				
450	450	Middle Cenomanian	Calcschist	180
1,078	1,078	Late Jurassic	Marl	220
1,454	1,454	Early Jurassic	Marl	240
1,585	1,585	Early Jurassic	Limestone	240
1,652	1,652	Late Aptian	Limestone	240
1,878	1,878	Late Aptian	Limestone	240
2,555	2,555	Late Triassic	Clay	280
3,005	3,005	Late Triassic	Clay	310
3,504	3,504	Stephanian?	Limestone	340
Chéraute-1 Well: Hyperextended Domain				
512	512	Cenomanian	Marl	240
1,010	1,005	Cenomanian	Marl	240
1,495	1,475	Senonian	Marl	270
2,032	1,982	Senonian	Marl	260
2,488	2,428	Senonian	Marl	270
3,014	2,924	Albian	Marl	260
3,495	3,375	Albian	Marl	290
3,995	3,841	Aptian	Marl	300
4,500	4,270	Aptian	Marl	300
4,974	4,644	Aptian	Marly limestone	330
5,507	5,002	Aptian	Marl	330
5,997	5,341	Late Jurassic	Marl	330
6,015	5,355	Late Jurassic	Marl	330
Uhart-Mixe-1 Well: Hyperextended Domain				
500	500	Senonian	Marl	230
613	613	Senonian	Marl	230
902	896	Senonian	Marl	240
952	946	Senonian	Marl	250
952	948	Senonian	Marl	250
1,264	1,254	Senonian	Marl	260
1,508	1,496	Early Cenomanian	Marl	270
1,735	1,722	Early Cenomanian	Marl	280

Table 2
Continued

Measured depth (m)	True vertical depth (m)	Age	Lithology	Raman temperature (°C)
1,777	1,764	Early Cenomanian	Marl	280
Bellevue-1 Well: European Necking Zone				
560	560	Cenomanian	Marl	120
1,180	1,180	Albian	Marl	140
1,550	1,550	Aptian	Limestone	160
2,040	2,037	Aptian	Marl	180
2,570	2,565	Barremian	Siltstone	200
3,000	2,992	Late Jurassic	Limestone	220
3,500	3,470	Middle Jurassic	Marl	230
4,000	3,934	Middle Jurassic	Limestone	240
4,180	4,101	Late Jurassic	Marl	240
4,690	4,560	Barremian	Limestone	280
4,730	4,596	Barremian	Limestone	240
5,210	5,050	Late Triassic	Clay	260
5,780	5,480	Late Triassic	Clay	300
6,430	6,238	Late Triassic	Clay	310
6,710	6,470	Barremian	Limestone	330
6,890	6,591	Barremian	Limestone	330
Les Cassieres-2 Well: European Proximal Margin				
535	535	Santonian	Marl	160
968	966	Santonian	Marl	200
1,492	1,488	Cenomanian	Marl	200
1,994	1,990	Cenomanian	Marl	200
2,510	2,505	Cenomanian	Marl	220
3,083	3,077	Aptian–Albian	Marl	240
3,580	3,560	Aptian–Albian	Marl	240
4,005	3,960	Aptian–Albian	Marl	270
4,523	4,443	Aptian–Albian	Marl	270
5,015	4,865	Aptian–Albian	Marl	300
Orthez-102 Well: European Proximal Margin				
510	500	Senonian	Calcschist	120
1,140	1,127	Senonian	Calcschist	140
2,000	1,979	Albian	Limestone	150
2,600	2,577	Aptian	Limestone	160
2,770	2,747	Aptian	Limestone	170
3,350	3,325	Barremian	Marl	200
4,030	3,995	Late Jurassic	Marl	220
4,200	4,156	Early Jurassic	Marl	240
4,260	4,214	Early Jurassic	Limestone	230
4,360	4,310	Senonian	Marl	240
4,390	4,338	Aptian	Marl	240
4,470	4,416	Barremian	Marl	120
4,690	4,632	Senonian	Marl	120
4,830	4,769	Albian	Marl	120
4,910	4,846	Albian	Marl	120
5,010	4,943	Albian	Marl	120
5,120	4,953	Aptian	Limestone	130
5,481	5,399	Aptian	Limestone	130

the same stratigraphic level, it was not possible to estimate a paleogeothermal gradient for this structural unit. We tried to estimate RSCM peak temperatures in the Cenomanian to Santonian carbonate platform deposits (Calcaires des Cañons limestones), but the samples are too recrystallized to yield reliable data.

5.2. Iberian Necking Zone

We calibrated RSCM peak temperatures in the Iberian necking zone from 33 outcrop samples from the Mendibelza (Figure 9a), Arbailles (Figure 9b), Saint-Etienne de Baïgorry, and Arberoue Units (Table 1) and cuttings from the Hasparren-101 well (Table 2). Ten samples were from Albian (synrift) to Santonian

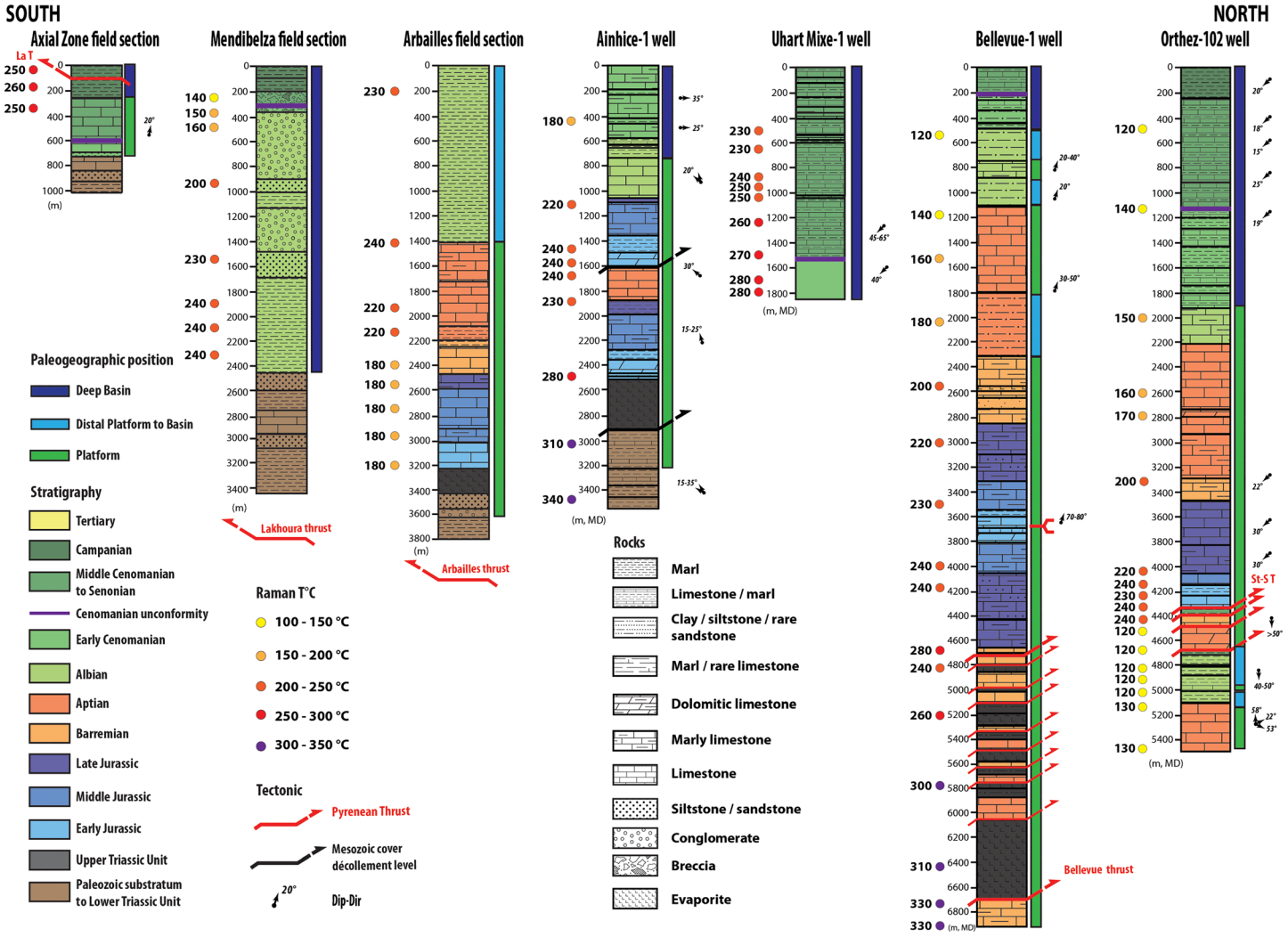

Figure 6. Columnar sections along a north-south transect including RSCM peak temperatures (Raman T°C), paleogeographic position, stratigraphy, tectonic, and lithology. The bars to the right of the columnar sections represent the paleogeographic position in the tectonic basin. MD = measured depth; St-ST = Sainte-Suzanne thrust. See Figure 2a for wells and field samples location.

(postrift) deposits of the Mendibelza Unit, for which a Mesozoic stratigraphic section 2,400 m thick has been reconstructed on the basis of new field observations and previously published data (Figure 6; Boirie, 1981; Saspiturry, 2019; Saspiturry, Razin, et al., 2019; Souquet et al., 1985). The 800 m section at the base of the Albian synrift sequence reached temperatures of 230–240°C, values that are consistent with those obtained by Clerc et al. (2012). RSCM peak temperatures decreased upward from 230 to 140–160°C in the upper Albian siltstone and Santonian breccia (Figure 7). The temperature difference between the base and the top of the Mendibelza section defines a linear regression line with R^2 = 0.95 defining a paleogeothermal gradient of 46°C/km (Figure 9a). To the west, six samples from the Saint-Etienne-de-Baïgorry Unit recorded the same range of RSCM peak temperatures (130–160°C) in samples from the top of the Mendibelza Unit section (Figures 3 and 5a).

Twelve samples from the Arbailles Unit represented Jurassic (prerift) to Albian (synrift) deposits (Figures 3 and 6). Surprisingly, the Jurassic to Barremian carbonate deposits, in the northern part, recorded a uniform RSCM peak temperature of 180°C whereas the younger Aptian and Albian carbonates and marls, in the southern part, recorded temperatures of 220–240°C (Figure 9b and Table 1). This range is close to the RSCM peak temperature range of 250°C and 256°C published by Clerc et al. (2012). The anomalous temperature distribution in the Arbailles Unit makes it difficult to estimate the paleogeothermal gradient there.

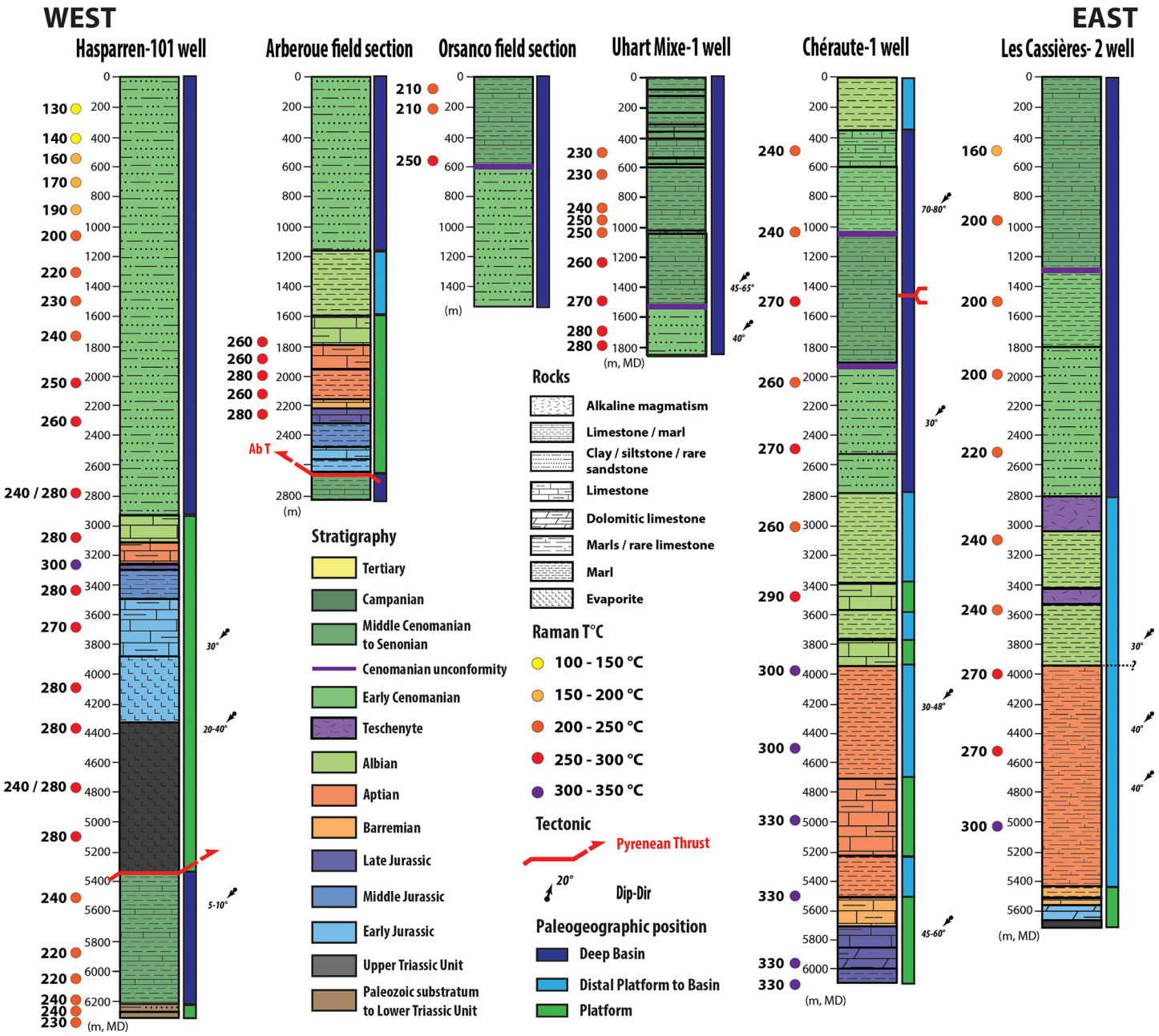

Figure 7. Columnar sections along a north-south transect including RSCM peak temperatures (Raman T°C), paleogeographic position, stratigraphy, tectonic, and lithology. The bars to the right of the columnar sections represent the paleogeographic position in the tectonic basin. MD = measured depth. See Figure 2a for wells and field samples location.

The site of the Hasparren-101 well was located between deltaic deposits to the west (Saint-Jean-de-Luz domain; Razin, 1989) and deep basin turbidites to the east (Saint-Palais domain; Souquet et al., 1985) during the Albian rifting stage. That position lies between the Iberian proximal margin and the deep turbiditic basin. This well penetrates two structural units separated by a major thrust at 5,400 m MD (Figure 7). The lower, autochthonous unit is made up of basement rocks and Permian red siltstone directly overlain by Turonian to Santonian carbonate turbidites. It yielded RSCM peak temperatures ranging from 220°C to 240 C (Figure 5b and Table 2). The tectonic contact between the two structural units is marked by a sharp paleotemperature gap of around 50°C. The upper, allochthonous unit is an Upper Triassic to Cenomanian sequence. The lower part of this unit yielded fairly uniform RSCM peak temperatures around 280°C

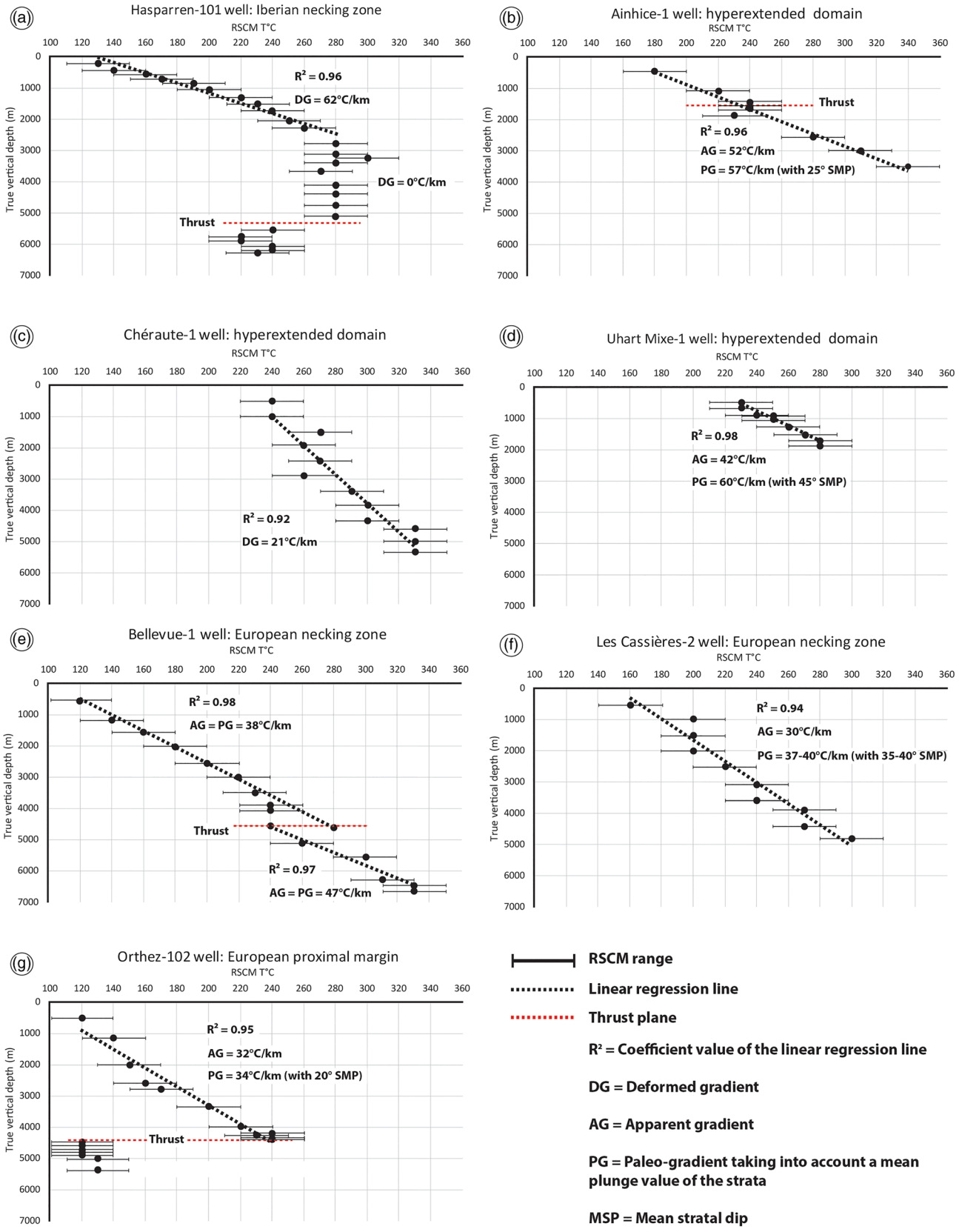

Figure 8. RSCM peak temperatures corrected for horizontal deviations (a) Hasparren-101 borehole, (b) Ainhice-1 borehole, (c) Chéraute-1 borehole, (d) Uhart-Mixe-1 borehole, (e) Bellevue-1 borehole, (f) Les Cassières-2 borehole, and (g) Orthez-102 borehole.

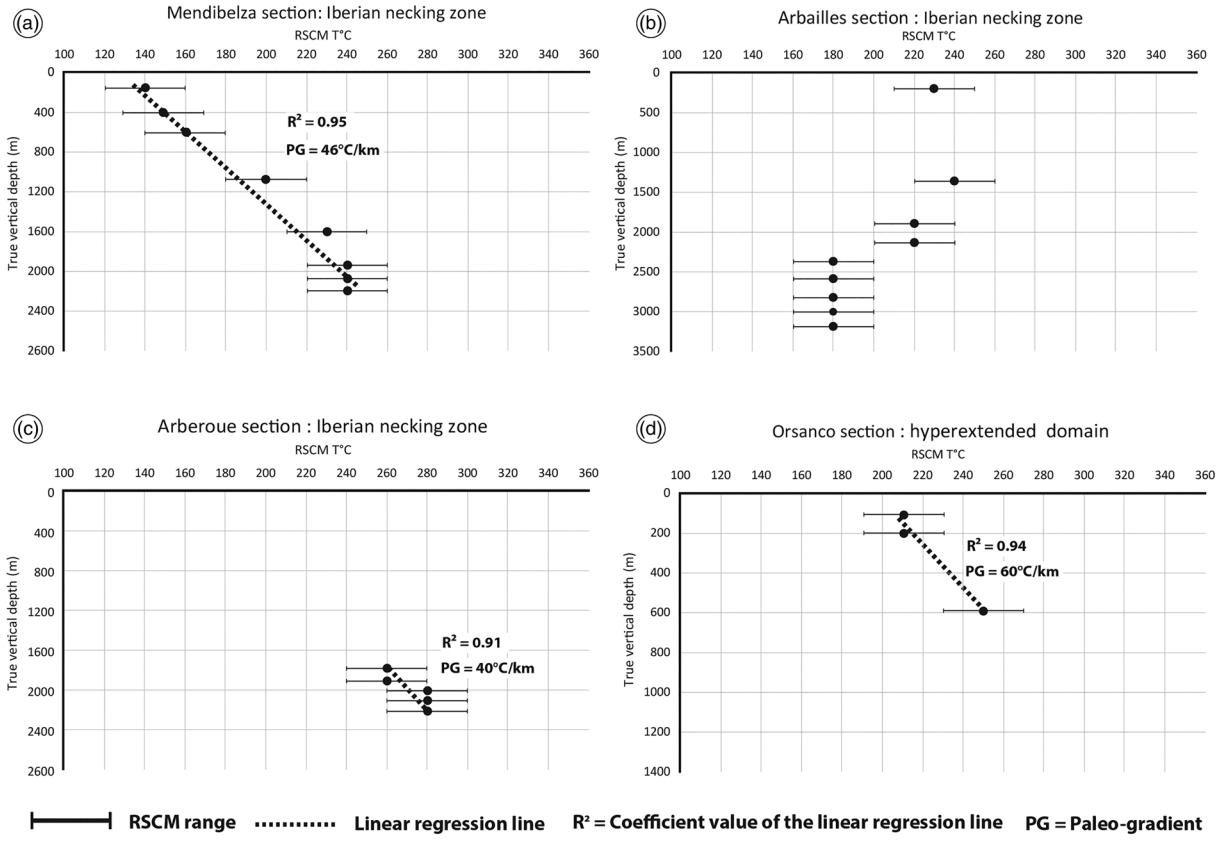

Figure 9. RSCM peak temperatures of field sections (a) Mendibelza, (b) Arbailles, (c) Arberoue, and (d) Orsanco sections.

between 2,800 and 5,400 m MD (Figure 7). This uniformity may reflect the presence of high-conductivity rocks such as evaporates, but these are not present in the depth range 2,800–3,900 m. Another explanation may lie in the possible presence of convective processes, which could occur if these formations (limestones, marls, and evaporites) are sufficiently permeable. Thermal convection could have homogenized temperatures over a thickness of more than 2,500 m. Raman spectra of the two samples from 2,790 and 4,760 m were heterogeneous, yielding RSCM peak temperatures of 240°C and 280°C, respectively (Figure 7 and Table 2). The upper part of the upper unit yielded RSCM peak temperatures varying from 280°C at the base to 130°C at the top. The resulting linear regression line defines a 62°C/km deformed thermal gradient (Figure 8a). The Hasparren-101 well is not included in the cross-section because (1) it is far from the cross-section line and (2) its upper unit is intensively tectonized and has variable stratal dips, thus estimating a paleogeothermal gradient based on a mean dip was problematic. However, this borehole has been integrated in this study as it bears upon the role of fluid circulation in controlling the local thermal record (see section 6.2.2).

The Arberoue field section is paleogeographically in the same domain as the Hasparren-101 well. The Arberoue succession, composed of Late Jurassic to Aptian carbonates, yielded RSCM peak temperatures, ranging from 260°C to 280°C, that are similar to those obtained from the Hasparren-101 well in the same stratigraphic interval (Figures 3a, 5a, and 7 and Table 1). The temperature difference between the base and the top of the Arberoue section defines a linear regression line with $R^2 = 0.91$ defining a paleogeothermal gradient of 40°C/km (Figure 9c).

5.3. Hyperextended Domain

Peak temperatures in the hyperextended domain of the Mauléon basin were determined from field samples and boreholes. The distal parts of the hyperextended domain are represented in the Orsanco section

(Figures 3a and 7 and Table 1), the outcrop samples HEL-1, IRI-1, and AGU-2, and the Ainhice-1, Chéraute-1, and Uhart-Mixe-1 wells.

The Ainhice-1 well reaches basement strata of Carboniferous (Stephanian) age at a depth of around 2,900 m MD (Figure 6). The Mesozoic cover is duplicated by a minor northward thrust at 1,600 m MD that was active during early Albian time (Figure 6; Saspiturry, Razin, et al., 2019). RSCM peak temperatures varied from 340°C at the base to 180°C at the top (Figures 5c and 8b and Table 2). These values fit a linear regression line corresponding to a 52°C/km apparent thermal gradient and, after correcting for a mean stratal dip of 25°, a paleogeothermal gradient of 57°C/km (Figure 8b). There is no significant variation in RSCM peak temperature across the décollement (Figure 8b).

The Chéraute-1 well penetrates a sequence of Jurassic to Upper Cretaceous rocks (Figure 7). The upper part of the well displays an Albian-Cenomanian cover sequence that is duplicated in reverse order above approximately 1,500 m MD of Upper Cretaceous deposits. The RSCM peak temperatures were more variable than in the other wells, ranging from 330°C to 290°C between 6,000 and 3,400 m MD (Figure 7 and Table 2). The folded Albian to Senonian sequence yielded RSCM peak temperatures of 240°C on top and 260–270°C at the base (Figures 5d and 7). These RSCM peak temperatures define a deformed thermal gradient of 21°C/km, although the linear regression line falls short of significance with $R^2 = 0.92$ (Figure 8c). The complex fold structure makes it difficult to estimate a reliable paleogeothermal gradient for this well.

The Uhart-Mixe-1 well penetrates Cenomanian to Turonian turbidites (Figures 3 and 6). The RSCM peak temperatures vary from 280°C at the base to 230°C at the top (Figures 5e and 6 and Table 2). These values fit a linear regression line defining an apparent thermal gradient of 42°C/km and a paleogeothermal gradient of 60°C/km after taking into account a 45° mean stratal dip (Figure 8d).

The Orsanco field section exposes the same paleogeographic domain as the Uhart-Mixe-1 well. Samples from that section yielded RSCM peak temperatures of 210–250°C, which are similar to those in the corresponding part of the Uhart-Mixe-1 well (Figure 3a and Table 1). The temperature difference between the base and the top of the Orsanco section defines a linear regression line with $R^2 = 0.94$ defining a paleogeothermal gradient of 60°C/km (Figure 9d).

Approximately 10 km west of the Orsanco section, outcrop samples HEL-1 and IRI-1, of Santonian age, yielded RSCM peak temperatures of 180°C and 200°C, respectively, and outcrop sample AGU-2 to their south, of Late Jurassic age, yielded a RSCM peak temperature of 160°C (Figure 3a and Table 1).

5.4. European Necking Zone

The paleotemperature of the European necking zone was derived from the Bellevue-1 and the Les Cassières-2 wells (Figures 3a and 6). The Bellevue-1 well penetrates a north directed major thrust around 4,700 m MD that divides the drilled interval into a basal and an upper unit.

The intensively deformed basal unit, made up of Upper Triassic evaporites and Barremian-Aptian carbonate lenses, is characterized by RSCM peak temperatures ranging from 330°C at the base (6,900 m MD) to 240°C on the thrust plane (Figures 5f and 8e). Despite the intense deformation, the RSCM values of this unit fit a linear regression line defining an apparent thermal gradient of around 47°C/km (Figure 8e). The tectonic contact between the basal and upper units corresponds to a temperature offset of 40°C.

The upper unit is repeated in reverse across an anticline affecting Jurassic to Albian carbonates and marls. This complex structure has been interpreted as the result of Tertiary reactivation of an Albian diapiric ridge (Saspiturry, Razin, et al., 2019). The upper unit yielded RSCM peak temperatures decreasing steadily from 280°C at the base to 120°C at the top (Figures 5f and 6 and Table 2). These temperatures fit a linear regression line defining an apparent thermal gradient of 38°C/km (Figure 8e).

The Bellevue fold is inherited from Albian-Cenomanian time, as it corresponds to a synrift diapir that controlled Albian sedimentation (Saspiturry, 2019). During the compression, the fold was thrusted northward along the Bellevue thrust. Thus, the fold is Albian in age and does not result from Pyrenean compression. It is thus older than the thermal event. RSCM peak temperatures in these two units define similar linear regression lines, meaning that the folded structure in the upper unit is clearly older than the thermal event that set the RSCM peak temperatures. In this case we cannot consider the structural data to restore the paleogeothermal gradient. However, the cross section (Figure 3b) shows that the northward Bellevue

thrust doesn't create major Pyrenean tilting at the site of the Bellevue-1 well. Consequently, the paleogeothermal gradient is the same as the apparent thermal gradients, that is, 47°C/km in the basal unit and 38°C/km in the upper unit.

The Les Cassières-2 well penetrates a complete succession of Jurassic to Santonian sediments, unaffected by any Tertiary thrust (Figure 7). The Aptian sequence yielded a RSCM peak temperature of around 300°C whereas the Santonian turbidites had a peak temperature of 160°C (Figures 5g and 7 and Table 2). These data define an apparent thermal gradient of 30°C/km (Figure 8f). Taking into account a mean stratal dip of 35–40°, the paleogeothermal gradient of this well is estimated at 37–40°C/km.

5.5. European Proximal Margin

The paleotemperatures of the European proximal margin were defined using data from the Orthez-102 well (Figure 3c). The Orthez-102 well penetrates two structural units separated by the Sainte-Suzanne northward thrust at 4,400 m MD. The lower autochthonous unit, made up of Aptian to Upper Cretaceous limestone and marl, yielded RSCM peak temperatures of 120–130°C (Figure 6). The upper allochthonous unit is a complete sequence of Jurassic limestone to Senonian carbonate turbidites. The base and top of the upper unit yielded RSCM peak temperatures of 240°C and 120°C, respectively (Figures 5h and 6), for an apparent thermal gradient of 32°C/km. Taking into account a mean stratal dip of 20°, the paleogeothermal gradient of this unit is estimated at 34°C/km.

5.6. Thermal Evolution of the Hyperextended Domain: Numerical Simulation

We derived a simplified model to constrain the thermal evolution of the Mauléon basin area since 120 Ma that was based on geological knowledge plus reasonable thermal properties and boundary conditions. This model allowed us to (1) validate the coherence of the paleogradient estimated by the RSCM methodology, (2) estimate at what date the maximum temperature was reached by a rock that underwent the series of tectonic events recorded in the Mauléon basin, (3) constrain the present-day mantle heat flow values beneath the basin, and (4) estimate the synrift mantle heat flow beneath the basin.

The model calculates the thermal evolution of a crustal section undergoing four stages as shown in Figure 10: (1) a thermal pulse and sedimentation stage featuring increasing mantle heat flow from 120 to 80 Ma at the base of a thinning crust (initially 30 km thick) representing both the rifting stage and the postrift stage (refer to Figure 2 and section 2.1 for details of the tectonic stages), (2) a thermal cooling stage coupled to a sedimentation event from 80 to 40 Ma representing the onset of compression in the Pyrenees, (3) a thermal warming stage from 40 to 15 Ma, corresponding to the main exhumation and erosional stage of the Pyrenees, and (4) a thermal relaxation stage from 15 Ma to the present, characterizing the postcollisional stage in the Pyrenees.

5.6.1. Numerical Approach

Our model incorporates the thickness of the different crustal units, as well as the sedimentation and erosional rates, from this and previous studies (e.g., Saspiturry, Razin, et al., 2019; Vacherat et al., 2014, and references therein). The main unknown variable is the mantle heat flow and its variation through time. However, the following constraints have been considered: a maximum RSCM peak temperature of 600°C extrapolated at a depth of 10 km, and a present-day estimated temperature gradient of 25.0 ± 2.7°C/km (see Supporting Information S1).

We assume that crustal extension was accompanied by a thermal pulse from 120 to 80 Ma. To simulate this pulse, a Gaussian-type horizontal profile is imposed at a depth of 30 km in the model:

$$Q_m = Q_{m0} \times \exp\left(-x^2/\lambda^2\right), \quad (1)$$

where Q_m is the mantle heat flow, Q_{m0} is its maximum value at the model center (horizontal distance $x = 0$), and λ is a characteristic width of the thermal pulse (the half width of the gaussian curve). Previous thermal models (Duretz et al., 2019; Jourdon et al., 2019, 2020) used different initial thermal regimes resulting in a thermal anomaly that is 50–100 km wide at Moho depth. Accounting for the gaussian shape of Q_m, we tested two values of λ, 25 and 75 km. The maximum heat flow Q_{m0} is constrained such that 600°C is reached at 10 km depth soon after the synrift stage (~80 Ma), as demonstrated by Vacherat et al. (2014) using low-temperature thermochronology analysis. After this heating phase, mantle heat flow decreases to a much lower value that is constrained by the present-day temperature gradient.

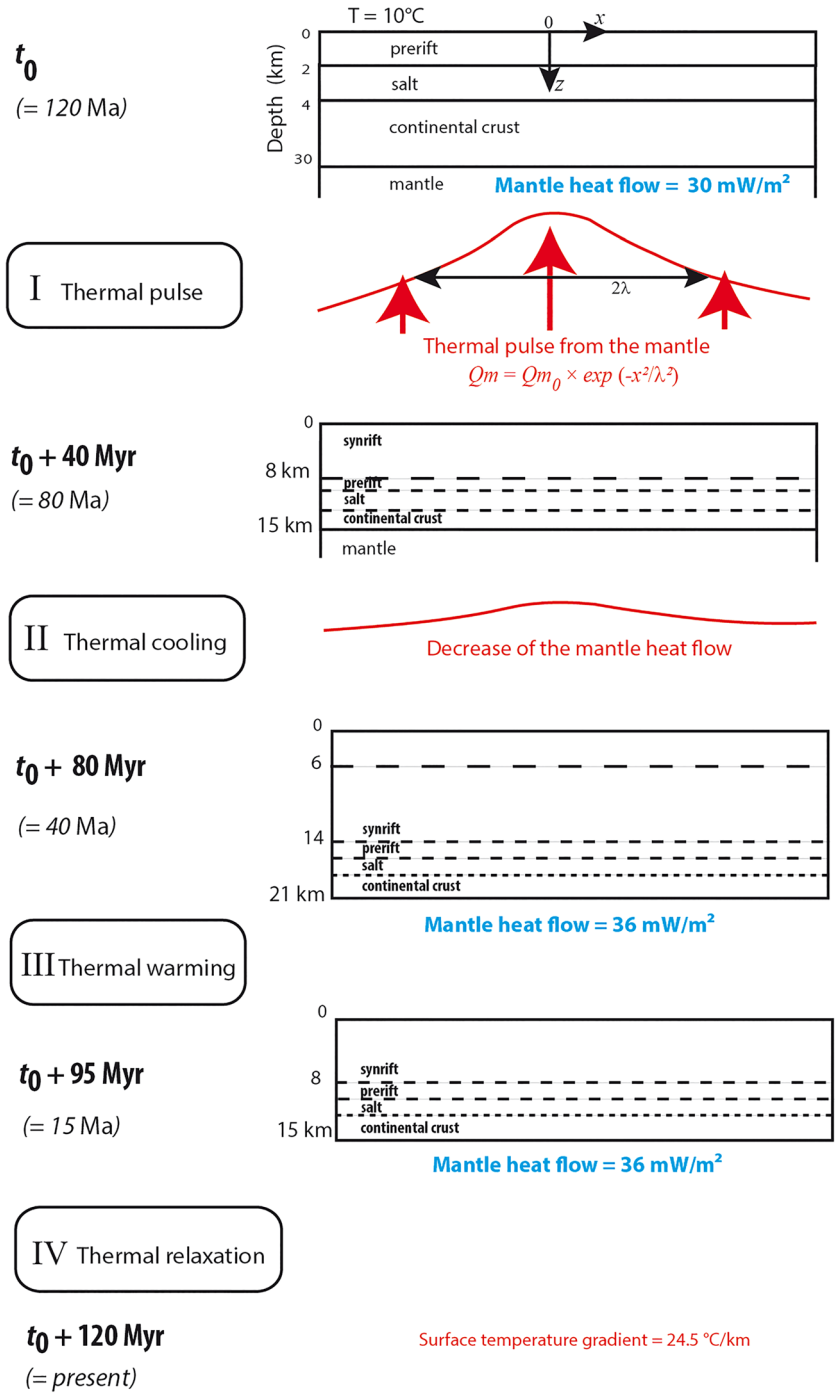

Figure 10. Conceptual model of the four stages of thermal events since 120 Ma of the Mauléon basin. Lithologies are shown but are not accounted for in thermal properties (see text). The final value of mantle heat flow (36 mW/m^2) accounts for present-day surface temperature gradients.

From a thermal point of view, an erosion event corresponds to the vertical upward motion of crustal material at a velocity corresponding to the erosion rate, and a sedimentation event corresponds to downward motion of crustal material at a velocity corresponding to the sedimentaton rate (e.g., Turcotte & Schubert, 2002, section 4–20). To simulate the thermal effects of sedimentation and erosion events, we used the advective term of the heat equation and assigned the erosion/sedimentation rate to the vertical velocity component.

Sedimentation is thus represented by a positive vertical velocity for the entire model, while erosion is assigned a negative velocity (the vertical axis being downward). Rates are calculated with the thicknesses and durations of erosion or sedimentation events shown in Figure 10.

5.6.2. Heat Equation, Boundary Conditions, and Thermal Properties

As illustrated in Figure 10, the top surface is considered fixed at $z = 0$. During the 120 million years (Myr) of thermal evolution, the underlying medium can move upward (during extension and erosion phases) or downward (during sedimentation). For a medium moving at velocity u (m/s), the heat equation is

$$\rho Cp \frac{\partial T}{\partial t} = \nabla\left(k\vec{\nabla}T\right) - \rho Cp\ \vec{u}\vec{\nabla}\vec{T}, \tag{2}$$

where ρ is density (kg/m^3), Cp is heat capacity (J/kg K), ∇ and $\vec{\nabla}$ are the divergence and gradient operators, T is temperature (K), t is time (s), and k is thermal conductivity (W/m K).

The chosen model box is 30 km thick, corresponding to the initial crustal thickness. The box length depends on the pulse wavelength: It is 80 km long for $\lambda = 25$ km but twice as long (160 km) for $\lambda = 75$ km. A fixed temperature condition ($T = 10$ °C) is imposed at the surface of the model. Lateral boundaries are insulating, and the basal boundary condition corresponds to a varying mantle heat flow. A fixed heat flow of 30 mW/m^2 is imposed at time $t = 0$ (or t_0, or 120 Ma). A thermal pulse (Equation 1) is imposed during the thinning phase (from t_0 to $t_0 + 40$ Myr, i.e., from 120 to 80 Ma). To reproduce the present-day surface temperature gradient, the mantle heat flow has to be decreased (Figure 10).

Because the thermal properties of different lithologies would yield only slight variations in the temperature distribution, we chose to assign the crust and the mantle a uniform composition with a temperature-dependent thermal conductivity. Given the high temperatures involved, it is more relevant to account for thermal effects on thermal conductivity and diffusivity (e.g., Braun, 2009) than to account for 1–2 km of salt within a typical continental crust. Accounting for the high thermal conductivity of a 2 km thick layer of salt would decrease temperatures by ~35°C, implying that a higher mantle heat flow would be required to reach 600°C at a depth of 10 km. Our final result for the inferred mantle heat flow value is thus a minimum estimate. The temperature-dependent law is given by (Clauser & Huenges, 1995)

$$k(T) = \frac{k(0)}{1.007 + T\left(0.0036 - \dfrac{0.0072}{k(0)}\right)}, \tag{3}$$

where $k(0)$ approximates the room-temperature thermal conductivity, taken here as 2.5 W/m K. Changes in this value govern the mantle heat flow value needed to meet the 600°C constraint; for example, a $k(0)$ value of 3.0 W/m K would require that the Q_{m0} value for $\lambda = 25$ km increases by 10%.

The heat capacity of the medium is 1,000 J/kg K, and its density is 3,000 kg/m^3. The heat production rate throughout the medium decreases exponentially according to

$$A(z) = A_0 \exp\left(-\frac{z}{D}\right), \tag{4}$$

where A_0 is 1.5 μW/m^3 and the depth scale D is assumed to be 13 km. These are reasonable values that produce an initial thermally stable crustal regime with a basal temperature of 535 °C and a surface heat flow of 48 mW/m^2.

5.6.3. Thermal Pulse

The mantle heat flow condition (Equation 1) is applied at the bottom of the modeled region, regardless of variations in the continental crust thickness, to avoid a spatially variable boundary condition. Hence, the thermal pulse imposed at a depth of 30 km is transferred to the moving base of the crust, as well as the advected heat component during the extension phase.

The heat equation was solved by the finite-element method with Comsol Multiphysics software, in which temperature-dependent properties can be easily implemented. Different values for the maximum mantle heat flow (Q_{m0}) were tested in order to reach 600°C at a depth of 10 km. For the small-scale thermal pulse ($\lambda = 25$ km), Q_{m0} is 100 mW/m^2, and for the large-scale thermal anomaly ($\lambda = 75$ km), Q_{m0} is 71 mW/m^2.

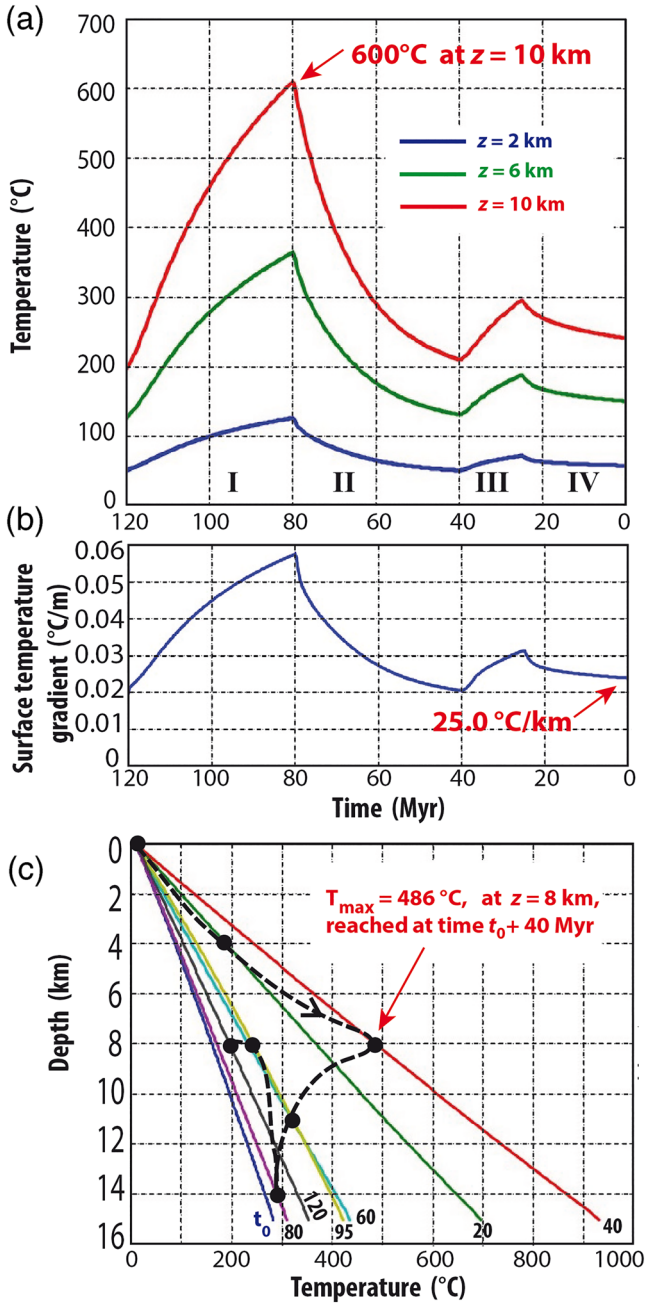

Figure 11. Model of the thermal evolution since 120 Ma based on model described in Figure 7, showing (a) temperature at three fixed depths, (b) temperature gradient at the surface, and (c) temperature-pressure path (dashed black line) for a rock (black dot) initially at the surface. Colored lines indicate model geotherms at various times from t_0 = 120 to 0 Myr.

In both cases, the maximum heat flow at the base of the crust (at time t_0 + 40 Myr) ranges between 90 and 100 mW/m^2, and the surface heat flow (which includes the radioactive component) is 135–140 mW/m^2, a value consistent with surface heat flow values measured in continental rift zones (e.g., Jaupart & Mareschal, 2007; Lucazeau et al., 2010).

5.6.4. Thermal Evolution

Figure 11 shows the thermal regime of the crust from 120 Ma to present. Temperatures at three distinct depths (Figure 11a) and evolution of surface temperature gradient (Figure 11b) are shown. Figure 11c shows the evolution of temperature profiles together with the pressure-temperature-time path followed by a rock initially at the surface. The case shown in Figure 11 corresponds to Q_{m0} = 100 mW/m^2, λ = 25 km and $k(0)$ = 2.5 W/m K.

The model goes through four thermal stages: (I) The increased mantle heat flow at the base of the crust warms the entire crust while the coeval sedimentation and extension events have much smaller effects; (II) the crust cools due to the decrease of mantle heat flow and the effect of the sedimentation event; (III) temperatures increase due to the erosion event; and (IV) temperatures decrease toward equilibrium.

As shown in Figure 11c, the maximum temperature recorded by rock that initially (at t_0) was at the surface (486°C at 8 km depth) is reached at the end of the heating phase (t_0 + 40 Myr). The only way to reach higher temperatures would be to consider much higher erosion rates, which are not supported by field data.

The surface temperature gradient above the thermal pulse (Figure 11b) shows that the present-day value (t_0 + 120 Myr) has recovered to its long-term value (25°C/km). Looking at time t_0 + 40 Myr (age 80 Ma), the surface temperature gradient reaches 58°C/km, close to the paleogradient estimate for the hyperextended domain. However, RSCM peak temperatures that were used for paleogradient estimates do not correspond to surface values. A closer look at the calculated paleogradients, from the surface to the bottom of the model, reveals that above the thermal pulse, the temperature gradient varies within a small range of 55 to 62°C/km, as inferred from RSCM peak temperatures.

6. Discussion

6.1. Age of RSCM Peak Temperature

In this study, we defined the thermal evolution of the Mauléon hyperextended rift on the basis of a thermal numerical simulation and RSCM peak temperatures, derived from 155 outcrop and borehole samples, that ranged from 120°C to 340°C. The younger age limit of this thermal peak is constrained by the late Santonian onset of rift inversion and the resultant lowering of the thermal gradient (Labaume et al., 2016; Vacherat et al., 2014). The youngest rocks analyzed by RSCM are of early Santonian age and record RSCM peak temperatures around 180°C. Because this temperature postdates the early Santonian, it does not reflect the synrift geothermal gradient but must be attributed to a later gradient associated with burial under synorogenic sediments. The thermal simulation not only confirms the RSCM peak temperatures methodology but also shows that the high paleogeothermal gradient in the Mauléon basin center was acquired during the Albian-Cenomanian rifting stage, also indicated by a low-temperature thermochronology analysis (Vacherat et al., 2014). This high paleogeothermal gradient is consistent with the presence of a positive gravity anomaly (Figure 1b; Boillot et al., 1973; Casas et al., 1997; Chevrot et al., 2018; Daignières et al., 1994;

Grandjean, 1992, 1994; Wehr et al., 2018), interpreted as the presence of subcontinental mantle at around 10 km depth (Figure 3b; Wang et al., 2016) that was locally exposed by denudation and reworked into the late Albian to early Cenomanian Urdach synrift deposits (Debroas et al., 2010; Fortané et al., 1986; Jammes et al., 2009; Lagabrielle et al., 2010; Roux, 1983) during the hyperextension of the continental crust (Masini et al., 2014; Teixell et al., 2016). The numerical simulation and the RSCM peak temperatures both indicate that the maximum peak temperature in the prerift to early postrift sediments was reached at the end of the postrift stage (~80 Ma). The low-temperature thermochronology analysis of the Mauléon basin by Vacherat et al. (2014) indicates that (1) the elevated Mauléon basin paleogeothermal gradient is inherited from the Albian-Cenomanian rifting stage and (2) rocks were heated to around 180°C soon after ~100 Ma and went through a nearly isothermal stage starting at ~80 Ma that lasted as long as ~30 Myr. This timing is also consistent with geochronological data from elsewhere in the North Pyrenean Zone, which put the peak at 107 and 85 Ma (Albarède & Michard-Vitrac, 1978b; Golberg et al., 1986; Golberg & Maluski, 1988; Montigny et al., 1986; Thiébaut et al., 1992). This high synrift gradient lasted at least through the postrift stage and possibly until 50 Ma, as proposed by Vacherat et al. (2014). As in the Mauléon basin, the Cameros basin in Spain has evidence of an elevated paleogeothermal synrift gradient in its deepest part (Golberg et al., 1988; Guiraud & Séguret, 1985; Rat et al., 2019). However, the high temperature-low pressure metamorphism reached its peak temperature during the postrift stage (Casas-Sainz & Gil-Imaz, 1998; Casquet et al., 1992; Golberg et al., 1988; Mata et al., 2001).

6.2. Synrift Paleogeothermal Gradient

6.2.1. Proximal Margins

The upper unit of the Orthez-102 well, in the European proximal margin, recorded a paleogeothermal gradient of 34°C/km. This gradient is consistent with the average geothermal gradient of ~30°C/km in continental domains and the average continental heat flow of 80 mW/m^2 (Jaupart & Mareschal, 2007). The isotherms in this borehole document northward transport of the warmer upper unit (240°C) over the cooler autochthonous unit (120°C). This latter RSCM peak temperature affects Aptian-Albian deposits of the autochthonous unit whereas the same stratigraphic levels of the allochthonous unit recorded higher RSCM peak temperatures of around 160–200°C. Consequently, we interpret the Orthez-102 autochthonous unit as representing a more proximal part of the European margin.

As mentioned in section 5.1, the paleogeothermal gradient could not be estimated for the Iberian proximal margin. The 15 Maastrichtian outcrop samples collected on the footwall of the Lakhoura thrust recorded RSCM peak temperatures of around 180°C in the Mendibelza domain (Figure 3a and Table 1). These temperatures are comparable to those obtained in the Cenomanian to Santonian breccias of the Lakhoura thrust hanging wall (140–160°C), but they affect younger sediments in the Lakhoura thrust footwall. Taking into account (1) the ~30°C/km thermal gradient of the proximal margin, (2) the temperature reached by the Santonian breccias in the Lakhoura thrust hanging wall (140–160°C), and (3) the regional thickness of the Campanian-Maastrichtian sedimentary pile, we can estimate the peak temperature reached by the eroded Maastrichtian sequence in the Lakhoura thrust hanging wall as around 100–120°C. This is lower than the peak temperatures in the Maastrichtian sequence of the Lakhoura thrust footwall (180°C). Thus, on the Iberian margin, the peak temperature largely postdates the rifting stage. This scenario is supported by thermochronology data (Bosch et al., 2016) showing that the region of Mendibelza and Lakhoura and both hanging wall and footwall cooled from 180°C or higher (U-Th/He on zircon) during early Eocene time, recording exhumation of the Lakhoura thrust domain while the Mauléon basin core reached peak temperatures soon after the rifting stage (Vacherat et al., 2014). However, thermochronology analyses constrain exhumation in the Lakhoura region during the Eocene but the age of Lakhoura thrust initiation is not resolved by these data and could be Late Santonian in age.

6.2.2. Necking Zones

The Iberian necking zone is represented by the Mendibelza (Figure 9a), Arbailles (Figure 9b), and Arberoue (Figure 9c) field sections and the Hasparren-101 borehole. This domain had higher paleogeothermal gradients than normal stable crust (30°C/km), 46°C/km in the Mendibelza section and 40°C/km in the Arberoue section. In the Arbailles field section, the RSCM peak temperature increases toward the younger stratigraphic levels, being 180°C in the Jurassic sequence and 230–250°C in the Albian synrift sequence. This increase could be interpreted as the result of early Cenomanian southward tilting of the Iberian necking

zone (Saspiturry, Razin, et al., 2019) that occurred before peak temperatures were reached. To the northwest, the Hasparren-101 borehole presents a more complex thermal record. The thrust plane at 5,380 m depth is marked by an abrupt 40°C change in the RSCM peak temperature from 240°C in the footwall to 280°C in the hanging wall (Figure 7). In our interpretation, this thrust transported a basinal section over a more proximal one.

The lower part of the allochthonous unit displayed an adiabatic temperature gradient over a 2.5 km interval with a constant 280°C temperature, whereas the upper part yielded a 62°C/km deformed thermal gradient (Figure 8a). As mentioned in section 4.2, the homogeneous temperature was probably due to upward circulation of hot fluid from 5.1 to 2.8 km (hot upwelling), but it could also correspond to downward circulation of cold fluid from 2.8 to 5.1 km (cold downwelling). Such temperature profiles, in which an elevated temperature gradient at the surface overlies a zone of constant temperature over several hundreds to thousands of meters, are often seen in geothermal systems typified by hot upwelling (e.g., Guillou-Frottier et al., 2013; Muraoka et al., 2000). However, in this borehole, we could not discriminate between hot upwelling and cold downwelling. Although the 62°C/km deformed thermal gradient was probably influenced by fluid transport, it is not necessarily higher than it would be with no fluid circulation. For example, in the case of a permeable medium where permeability is depth-dependent, the surface temperature gradient over a zone of cold downwelling may be lower than the purely conductive case (see supporting information Text S2). It is thus problematic to estimate a paleogeothermal gradient in the presence of a convective zone.

In the European necking zone, the paleogeothermal gradient was estimated using the Bellevue-1 borehole just north of the Saint-Palais thrust (Figure 3a). The Bellevue-1 well intersects a complex structure corresponding to the Tertiary reactivation of an Albian diapiric ridge (Saspiturry, Razin, et al., 2019). The apparent thermal gradient shows, however, that the RSCM peak temperatures postdate the formation of this structure. Thus, we considered the paleogeothermal gradient to be very close to the apparent gradients or 38°C/km in the allochthonous unit and 47°C/km in the autochthonous unit (Figure 8e). These values are comparable to those obtained in the Iberian necking zone.

The Les Cassières-2 well, in the European necking zone, penetrates a well-preserved sedimentary succession undisturbed by major Pyrenean thrusting (Figure 3a). We consider it as a reference section for the European necking zone that defines a paleogeothermal gradient of ~37–40°C/km.

6.2.3. Hyperextended Domain

The paleothermal structure of the hyperextended domain was calibrated using the Chéraute-1, Uhart-Mixe-1, and Ainhice-1 boreholes (Figure 3a) and the Orsanco field section (Figure 9d). The Chéraute-1 borehole is just east of the Saison structure that accommodates the major Roquiague diapir (Figure 3a; Canérot, 1988, 1989, 2008). We interpret the fold in this well as having been induced by the development of the Roquiague diapir during Senonian time (Figure 7). The well is characterized by a steady rise in RSCM peak temperatures from 240°C to 330°C across a sedimentary succession 5,350 m thick, defining a deformed thermal gradient of 21°C/km (Figure 8c and Table 2). Heat refraction by thermally conductive Upper Triassic evaporites could be responsible for the homogenization of temperatures across the sedimentary basin infill near this structure. Consequently, the measured paleogeothermal gradient is incompatible with the gradients in the Uhart-Mixe-1 and Ainhice-1 wells. These two boreholes lie between the Saint-Jean-Pied-de-Port and Saison transfer zones (Figure 1; Canérot, 2008). The Ainhice-1 well, located at the transition with the Iberian necking zone, yielded an unusually high paleogeothermal gradient of 57°C/km (Figure 8b). Because the paleogeothermal profile was not disturbed where a packet of strata ~400 m thick was duplicated above the décollement at 1,600 m, the peak temperatures there clearly postdate the displacement on the décollement. The Uhart-Mixe-1 well, in the heart of the hyperextended domain, is free of major Pyrenean deformation. It too yielded an unusually high paleogeothermal gradient of 60°C/km (Figure 8d), as did the Orsanco field section (Figure 9d).

6.3. The Mauléon Basin Internal Metamorphic Zone

Considering the 60°C/km paleogeothermal gradient obtained using the RSCM peak temperatures in the Uhart-Mixe-1 well (Figure 8d), which is fully consistent with the gradient proposed on thermochronological grounds by Vacherat et al. (2014), we can extrapolate the temperature from the base of the well into the hyperextended domain in this sector of the Mauléon basin, between the Saint-Jean-Pied-de-Port and Saison transfer faults (Figure 1c) and estimate that the prerift cover reached a temperature of 500–600°C

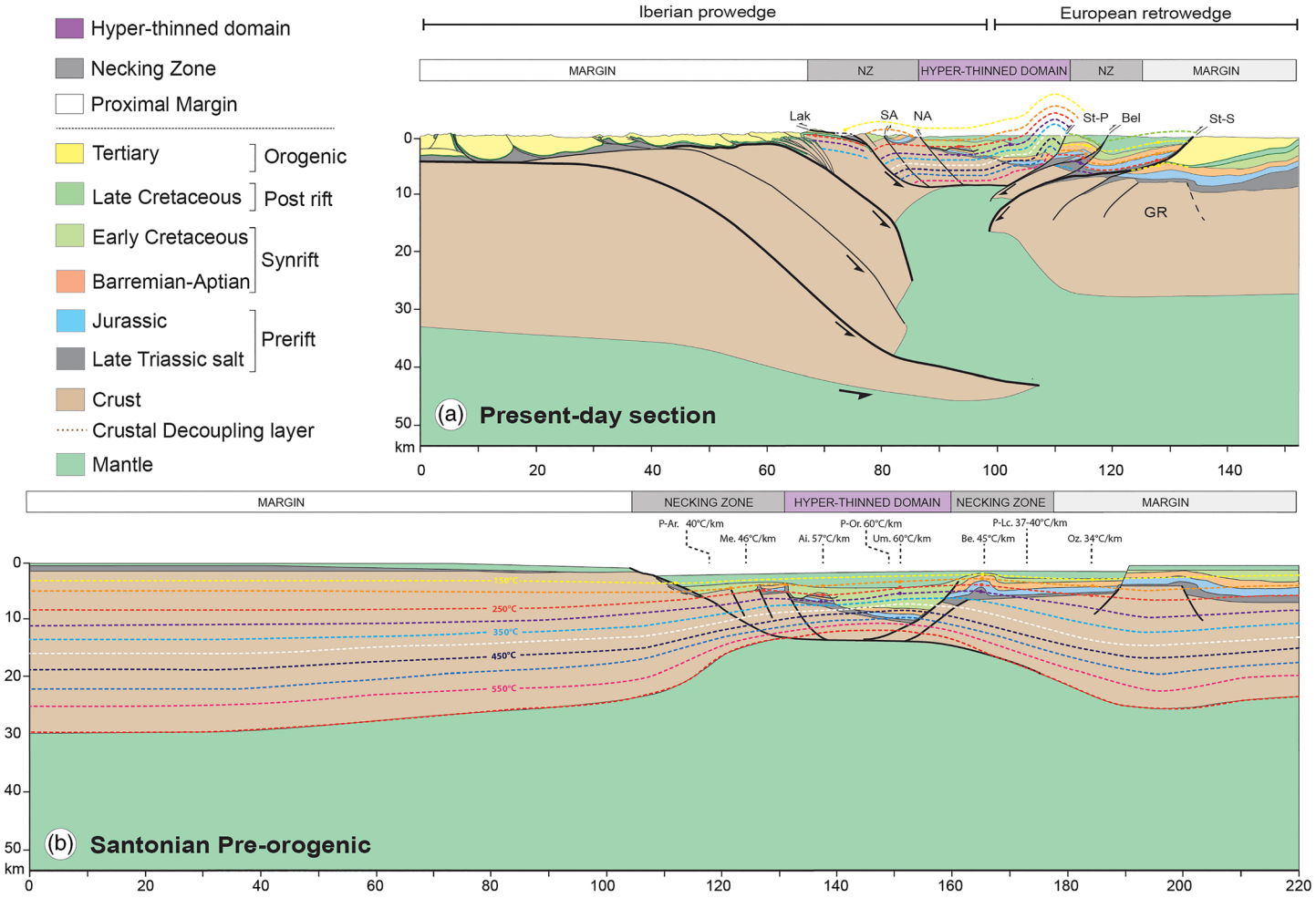

Figure 12. (a) Cross section through the modern Mauléon basin (Saspiturry, Allanic, et al., 2020). Thick-skin tectonics affecting the Iberian margin is responsible for postcollisional thermal heating, whereas the European margin is characterized by northward displacement of metamorphosed material and an unusually low postcollisional thermal gradient. (b) Late Cretaceous palinspastic restoration along a N-S cross section of the Mauléon basin (Saspiturry, Allanic, et al., 2020), displaying the synrift paleogeothermal gradients for the different structural margin domains. The Mauléon rift is characterized by a basinward increase of the paleogeothermal gradient, which induced a complex competition between brittle versus ductile deformation during early Cenomanian detachment on the Lakhoura fault (heavy black lines). Extension on the Saint-Palais detachment (dashed line) occurred during Albian time. P-Ar projected Arberoue section; Me section, Mendibelza; Ai, Ainhice-1 borehole; P-Or projected Orsanco section; Um, Uhart-Mixe-1 borehole; P-Lc, projected Les Cassières-2 borehole; Be, Bellevue-1 borehole; Oz, Orthez-102 borehole; Gr, Grand Rieu; Lak, Lakhoura thrust; SA, South-Arbailles thrust; NA, North-Arbailles thrust; St-P, Saint-Palais thrust; Bel, Bellevue thrust; St-S, Sainte-Suzanne thrust.

(Figure 12). This estimate is supported by the thermal simulation that indicated a maximum temperature of 600°C at the base of the Mauléon basin prerift cover. This temperature range is similar to those documented in the Internal Metamorphic Zone in the central and eastern Pyrenees (e.g., Azambre et al., 1992; Bernus-Maury, 1984; Chelalou et al., 2016; Clerc, 2012; Clerc et al., 2015; Golberg & Leyreloup, 1990; Vauchez et al., 2013) and the Nappes des Marbres in the Basque-Cantabrian basin (Ducoux, 2017; Lamare, 1936; Martínez-Torres, 1989; Mendia & Ibarguchi, 1991). The Internal Metamorphic Zone has been interpreted as the inverted base of the North Pyrenean hyperextended rift domain (Clerc, 2012; Clerc et al., 2015; Clerc & Lagabrielle, 2014; Ducoux, 2017; Lagabrielle et al., 2016). Consequently, we can infer that marble corresponding to the Internal Metamorphic Zone marbles exists in this sector of the Mauléon basin. However, farther eastward, the base of the basin does not exceed 350°C, as indicated by RSCM peak temperatures in the Chaînons Béarnais prerift cover (Corre, 2017) and Paleozoic basement (Asti et al., 2019). Contrary to the great east-west extent of the Internal Metamorphic Zone in the central and eastern Pyrenees, its extension in the Mauléon basin appears to be restricted to a very small area. Thus,

we can deduce that the Internal Metamorphic Zone hyperextended basin was much wider than the hyperextended Mauléon system, raising a question about the way Cretaceous extension is distributed along the Pyrenean rift system.

6.4. Distribution of the Synrift Paleogeothermal Gradient and Implications

The paleogeothermal gradients we obtained vary in the different structural units of the inverted hyperextended Mauléon basin. This variation is clearly evident along a proximal-distal margin transect: the Cretaceous paleogeothermal gradient increases basinward from ~34°C/km near the European proximal margin to ~37–47°C/km in the two necking zones to 57–60°C/km in the hyperextended domain (Figure 12b). The distribution of synrift paleogeothermal gradients is similar in the Camèros basin in Spain, where the rifting stage developed under a high thermal gradient (~70°C/km) in the basin core (Del Río et al., 2009; Mata et al., 2001). As in the Mauléon basin, the paleothermal gradient decreases to 41.5°C/km near the edge of the Camèros basin, along with the intensity of the high temperature–low pressure metamorphism (Omodeo-Salé et al., 2017). In the Mauléon basin, Lescoutre et al. (2019) and Lescoutre et al. (2019) have proposed that the paleogeothermal gradient had an asymmetric distribution in response to Early Cretaceous simple shear thinning. However, this study indicates that the Cretaceous paleogeothermal gradient was symmetric. This gradient is responsible for differing deformation styles across the basin that resulted in the formation of a pseudo-symmetric smooth-slope type extensional basin (Lagabrielle et al., 2020) in which the proximal margins underwent brittle deformation while the distal hyperextended domain underwent dominantly ductile thinning. This bimodal deformation style was linked to the basinward increase in the thermal gradient and burial of the central basin under thick sedimentary cover. The movement of the thick prerift sedimentary cover and synrift sediments into the hyperextended domain, aided by salt tectonics, accentuated the existing thermal gradient and led to ductile thinning of the upper continental crust under high-temperature/low-pressure metamorphic conditions at temperatures higher than 450°C (Lagabrielle et al., 2020).

6.5. Role of Rift Inheritance on Postcollisional Thermal Imprint

The Pyrenean compression on the Mauléon basin was not intense (Figures 1c and 12), and high-temperature marbles were not removed from the base of the hyperextended domain on the Saint-Palais thrust on its northern edge. Indeed, using numerical modeling, Jourdon et al. (2019) have shown that folding was limited for two reasons: (1) The deformation in the sedimentary cover was decoupled from the basement by Triassic evaporites, and (2) the position of the Mauléon basin in the Pyrenean retro-wedge led to its tectonic inversion being less pronounced, resulting in good preservation of precollision markers. Moreover, rift inversion started during late Santonian to Campanian time in the eastern Pyrenees (Choukroune & Etude Continentale et Océanique par Réflexion et réfraction Sismiques [ECORS] Team, 1989; Ford et al., 2016; Macchiavelli et al., 2017; Muñoz, 1992; Ternois et al., 2019) and in late Eocene time in the western Pyrenees (Labaume et al., 2016; Teixell, 1993). This asynchronous compression should have resulted in greater shortening in the central and eastern Pyrenees (Beaumont et al., 2000; Mouthereau et al., 2014; Muñoz, 1992; Vergés et al., 1995) than in the western Pyrenees (Teixell, 1996, 1998). Consequently, in the central and eastern Pyrenees, the Internal Metamorphic Zone was uplifted and exposed during Pyrenean compression whereas it is still buried in the Mauléon basin.

The previously acquired postrift isotherms were folded and tilted inside the Mauléon basin pop-up structure, bounded on the north by the Bellevue and Sainte-Suzanne thrusts and on the south by the Lakhoura thrust (Figure 12a). On the European margin, our evidence demonstrates that the postrift isotherms were not erased by the Pyrenean thrusting but instead were passively transported onto the proximal margin. On the Iberian margin, the Lakhoura thrust is marked by an increase of peak temperatures on its footwall, meaning that these peak temperatures were acquired after the thrusting.

The different thermal responses on the opposite sides of the pop-up structure can be linked to their tectonic reactivation style. Indeed, exhumation is limited in the northern retro-wedge, which was affected by thin-skinned deformation on an Upper Triassic salt décollement, and significantly greater in the southern pro-wedge, which underwent thick-skinned deformation (Figure 12a; Jourdon et al., 2019, 2020; Saspiturry, Allanic, et al., 2020). The post thrusting thermal structure along the Lakhoura thrust system was preserved due to sequential activation of thrusting southward and below the Lakhoura thrust system. This explanation

is consistent with thermochronology data (Bosch et al., 2016) showing that the basement was buried at 5–6 km depth at 30 Ma. Subsequently, deformation propagated southward and the Axial Zone was exhumed more than the North Pyrenean Zone.

On the European margin and in the hyperextended domain of the Mauléon basin, a major decrease in the thermal gradient to the 25.0 ± 2.7°C/km gradients in modern boreholes (see supporting information S1) followed the onset of compression. In the Iberian margin, the northward motion of the Iberian slab under the Mauléon hyperextended domain greatly decreased the heat flow from the asthenosphere. The European margin, to the contrary, never underwent thick-skin tectonics, explaining the current Moho depth of ~27 km there (Figure 12b). Instead, shortening of the European margin was accommodated by the Bellevue and Sainte-Suzanne thin-skin thrusts. The unusually low thermal gradient there is directly controlled by the thickness of the European continental crust and the presence of nonradiogenic subcontinental mantle at shallow depths.

6.6. Implications for Petroleum Systems

The peak temperature of rocks is a key parameter in the thermal evolution of basins. Many geothermometers, such as illite crystallinity, fluid inclusion microthermometry, and vitrinite reflectance, are not easily applicable in continental margin contexts such as the inverted Pyrenean system. In this study, we propose an integrated thermal approach, combining new analytical (RSCM thermometry) and numerical methods, to reconstruct the thermal history of hyperextended rift systems. The Mauléon inverted hyperextended basin represents an analog of current tectonostratigraphic settings targeted by petroleum companies; thus, its thermal evolution is of broad interest. Indeed, laboratory and numerical experiments directed at thermal interactions between the conducting continental crust and the convective mantle (e.g., Grigné et al., 2007; Guillou & Jaupart, 1995) have long indicated the presence of high heat flows and thermal gradients at continental margins. The insulating tendency of continents favors low mantle heat flow (10–20 mW/m^2) in intracontinental settings and much higher mantle heat flows at continental margins (more than 80 mW/m^2; e.g., Nirrengarten et al., 2019). Our study shows that continental margins have high mantle heat flows of ~100 mW/m^2 at the base of the hyperextended domain, as indicated by our basin thermal modeling (section 5.6). This high mantle heat flow is consistent with the 55–60°C/km thermal gradient, acquired at the end of the rifting stage, estimated by RSCM thermometry and thermal modeling. These values are consistent with other estimated paleotemperature gradients in continental rifts, which range from 50 to 100°C/km in Antarctica (Berg et al., 1989), 80–100°C/km in Iceland (Bertani, 2017), and 70°C/km in Spain (Del Río et al., 2009; Mata et al., 2001). Our estimated paleogeothermal gradients for the Mauléon hyperextended domain are comparable to other recent estimates: An estimate of 60–75°C/km by Corre (2017) was based on RSCM data, and estimates of 80°C/km by Vacherat et al. (2014) and Hart et al. (2017) were based on detrital zircon fission-track data and (U-Th-Sm)/He thermochronology data, respectively. In the Mauléon basin, the prerift cover was heated to temperatures as high as 500°C in the hyperextended domain and 150–200°C in the proximal margin. Thus, potential source rocks are overmature in the hyperextended domain and within the oil to gas window near the basin margins at the end of the rifting stage.

7. Conclusion

In this study, we estimated the paleothermal structure of the Mauléon hyperextended rift, using thermal numerical simulation and RSCM peak temperatures obtained from 155 outcrop and borehole samples. The Mauléon basin recorded an unusually high heat flow following Albian-Cenomanian hyperextension. Although the basin's elevated paleogeothermal gradient is inherited from the Albian-Cenomanian rifting stage, the numerical simulation and the RSCM peak temperatures indicate that the prerift to early postrift sediments reached their maximum temperature at the end of the postrift stage (~80 Ma). Thus, peak temperature postdates hyperextension, and the prerift to postrift sedimentary infill was thus affected by a paleogeothermal gradient whose isotherms crosscut all older tectonic structures.

The paleogeothermal gradients estimated in this study probably reached their maximum during Paleocene to early Eocene time. They rise in magnitude from the proximal domains to the center of the Albian-Cenomanian rift, starting from ~34°C/km on the European proximal margin (typical of stable cratons) to ~37–47°C/km in the two necking zones and to 57–60°C/km in the hyperextended domain. This finding is

strengthened by the numerical simulation that reveals temperature gradients above the thermal pulse varying within a small range (55–62°C/km). The area of highest gradient corresponds to the position of a positive gravity anomaly, interpreted as the presence at shallow depth (~10 km) of subcontinental mantle. Extrapolating the temperature at the base of the hyperextended domain, we infer that it reached 500–600°C in the segment of the basin between the Saint-Jean-Pied-de-Port and Saison transfer faults. These temperatures are similar to those measured in marbles of the Internal Metamorphic Zone in the central and eastern Pyrenees. However, the east-west divisions of the Mauléon basin high temperature are very narrow compared to those of the Internal Metamorphic Zone of the central and eastern Pyrenees. This finding suggests that the Albian-Cenomanian Metamorphic Internal Zone hyperextended basin was much wider than in the western Pyrenees.

The pop-up structures on the northern and southern flanks of the Mauléon basin, formed during later compression across the rift, present differing postcollisional thermal responses. The European margin was affected by northward thrusting that transported the paleoisotherms across the proximal margin without heating the thrust footwalls, a sign that the shortening rate was slow or that erosion was intense during the compression. As a result, the precollisional maximum paleogeothermal gradients of both the hyperextended domain and the European margin were preserved. On the Iberian margin, the geothermal gradient increased as the footwall of the Lakhoura thrust underwent heating after the collision, which reset its precollisional paleogeothermal record. This gradient increase can be linked to thickening of the Iberian continental crust following the formation of the antiformal crustal stack in the Axial Zone. The northward motion of the Iberian slab beneath the Mauléon hyperextended domain is responsible for a steep decrease in the asthenospheric heat flow and explains the low postcollisional geothermal gradient (25.0 ± 2.7°C/km) in the Mauléon basin core and European margin. Unlike the Iberian margin, the European margin never underwent thick-skinned tectonics and retained its current Moho depth of 25–27 km. Its low geothermal gradient is the consequence of a thin European continental crust and the presence at shallow depth of nonradiogenic subcontinental mantle.

Data Availability Statement

Data sets for this research are available in a Mendeley Data repository (https://data.mendeley.com/datasets/47kgv7r9wm).

Acknowledgments

This work is part of the Orogen geological research project cofunded by Total S.A., BRGM, and Institut national de sciences de l'Univers (INSU). We thank Orogen project managers Emmanuel Masini (Total), Olivier Vidal (CNRS), and Isabelle Thinon (BRGM). Review comments by Patrice Baby, Juan Contreras and three anonymous reviewers, and Djordje Grujic and Laurent Jolivet of the editorial board significantly improved the initial manuscript.

References

Albarède, F., & Michard-Vitrac, A. (1978a). Age and significance of the North Pyrenean metamorphism. *Earth and Planetary Science Letters*, *40*(3), 327–332. https://doi.org/10.1016/0012-821X(78)90157-7

Albarède, F., & Michard-Vitrac, A. (1978b). Datation du métamorphisme des terrains secondaires des Pyrenees par les méthodes ^{39}Ar-^{40}Ar et ^{87}Rb-^{87}Sr; ses relations avec les peridotites associées. *Bulletin de la Société Géologique de France*, *7*, 681–687. https://doi.org/10.2113/gssgfbull.s7-xx.5.681

Alhamawi, M. (1992). *Sédimentologie, pétrographie sédimentaire et diagenèse des calcaires du crétacé supérieur de la marge ibérique, vallée d'Ossau, vallée d'Aspe, Haute Chaîne, Pyrénées Atlantiques* (Doctoral dissertation, p. 356). Bordeaux 1.

Angrand, P., Ford, M., & Watts, A. B. (2018). Lateral variations in foreland flexure of a rifted continental margin: The Aquitaine basin (SW France). *Tectonics*, *37*, 430–449. https://doi.org/10.1002/2017TC004670

Aoya, M., Kouketsu, Y., Endo, S., Shimizu, H., Mizukami, T., Nakamura, D., & Wallis, S. (2010). Extending the applicability of the Raman carbonaceous material geothermometer using data from contact metamorphic rocks. *Journal of Metamorphic Geology*, *28*(9), 895–914. https://doi.org/10.1111/j.1525-1314.2010.00896.x

Arnaud-Vanneau, A., Arnaud, H., Charollais, J., Conrad, M.-A., Cotillon, P., Ferry, S., et al. (1979). Paléogéographie des calcaires urgoniens du sud de la France. *Géobios*, *3*, 363–383.

Aslanian, D., & Moulin, M. (2013). Palaeogeographic consequences of conservational models in the South Atlantic Ocean. *Geological Society of London, Special Publication*, *369*, 75–90. https://doi.org/10.1144/SP369.5

Aslanian, D., Moulin, M., Olivet, J.-L., Unternehr, P., Matias, L., Bache, F., et al. (2009). Brazilian and African passive margins of the Central Segment of the South Atlantic Ocean: Kinematic constraints. *Tectonophysics*, *468*, 98–112. https://doi.org/10.1016/j.tecto.2008.12.016

Asti, R., Lagabrielle, Y., Fourcade, S., Corre, B., & Monié, P. (2019). How do continents deform during mantle exhumation? Insights from the northern Iberia inverted paleopassive margin, western Pyrenees (France). *Tectonics*, *38*, 1666–1693. https://doi.org/10.1029/2018TC005428

Azambre, B., & Monchoux, P. (1998). Métagabbros amphiboliques et mise en place crustale des lherzolites des Pyrénées (France). *Comptes Rendus de l'Académie des Sciences-Series IIA-Earth and Planetary Science*, *327*, 9–15.

Azambre, B., & Rossy, M. (1976). Le magmatisme alcalin d'âge crétacé, dans les Pyrénées occidentales et l'Arc basque; ses relations avec le métamorphisme et la tectonique. *Bulletin de la société Géologique de France*, *7*, 1725–1728. https://doi.org/10.2113/gssgfbull.s7-xviii.6.1725

Azambre, B., Rossy, M., & Albarède, F. (1992). Petrology of the alkaline magmatism from the Cretaceous North-Pyrenean rift zone (France and Spain). *European Journal of Mineralogy*, *4*(4), 813–834. https://doi.org/10.1127/ejm/4/4/0813

Bai, Y., Dong, D., Brune, S., Wu, S., & Wang, Z. (2019). Crustal stretching style variations in the northern margin of the South China Sea. *Tectonophysics*, *751*, 1–12. https://doi.org/10.1016/j.tecto.2018.12.012

Beaumont, C., Muñoz, J. A., Hamilton, J., & Fullsack, P. (2000). Factors controlling the Alpine evolution of the central Pyrenees inferred from a comparison of observations and geodynamical models. *Journal of Geophysical Research*, *105*(B4), 8121–8145. https://doi.org/10.1029/1999JB900390

Beltrando, M., Manatschal, G., Mohn, G., Dal Piaz, G. V., Brovarone, A. V., & Masini, E. (2014). Recognizing remnants of magma-poor rifted margins in high-pressure orogenic belts: The Alpine case study. *Earth Science Reviews*, *131*, 88–115. https://doi.org/10.1016/j.earscirev.2014.01.001

Berg, J. H., Moscati, R. J., & Herz, D. L. (1989). A petrologic geotherm from a continental rift in Antartica. *Earth and Planetary Science Letters*, *93*(1), 98–108. https://doi.org/10.1016/0012-821X(89)90187-8

Bernus-Maury, C. (1984). *Etude des paragéneses caractéristiques du métamorphisme mésozoïque dans la partie orientale des Pyrénées* (Doctoral dissertation). Paris: Pierre et Marie Curie.

Bertani, R. (2017). *Perspectives for geothermal energy in Europe* (p. 304). Italy: World Scientific.

Beyssac, O., Goffé, B., Chopin, C., & Rouzaud, J. N. (2002). Raman spectra of carbonaceous material in metasediments: A new geothermometer. *Journal of Metamorphic Geology*, *20*(9), 859–871. https://doi.org/10.1046/j.1525-1314.2002.00408.x

Bodinier, J., Menzies, M. A., Shimizu, N., Frey, F. A., & McPherson, E. (2004). Silicate, hydrous and carbonate metasomatism at Lherz, France: Contemporaneous derivatives of silicate melt–harzburgite reaction. *Journal of Petrology*, *45*(2), 299–320. https://doi.org/10.1093/petrology/egg107

Bodinier, J. L., Dupuy, C., & Dostal, J. (1988). Geochemistry and petrogenesis of Eastern Pyrenean peridotites. *Geochimica et Cosmochimica Acta*, *52*(12), 2893–2907. https://doi.org/10.1016/0016-7037(88)90156-1

Boillot, G., Capdevilla, R., Hennequin-Marchand, I., Lamboy, M., & Lepretre, J. P. (1973). La zone nord-pyrénéenne, ses prolongements sur la marge continentale nord-espagnole et sa signification structurale. *Comptes Rendus de l'Academie des Sciences (Paris)*, *227*, 2629–2632.

Boillot, G., Féraud, G., Recq, M., & Girardeau, J. (1989). Undercrusting by serpentinite beneath rifted margins: The example of the west Galicia margin (Spain). *Nature*, *341*(6242), 523–525. https://doi.org/10.1038/341523a0

Boillot, G., Recq, M., Winterer, E. L., Meyer, A. W., Applegate, J., Baltuck, M., et al. (1987). Tectonic denudation of the upper mantle along passive margins: A model based on drilling results (ODP leg 103, western Galicia margin, Spain). *Tectonophysics*, *132*(4), 335–342. https://doi.org/10.1016/0040-1951(87)90352-0

Boirie, J.-M. (1981). *Etude Sédimentologique des Poudingues de Mendibelza (Pyrénées Atlantiques)* Doctoral dissertation. Toulouse: Université Paul Sabatier de Toulouse (Sciences).

Bosch, G. V., Teixell, A., Jolivet, M., Labaume, P., Stockli, D., Domènech, M., & Monié, P. (2016). Timing of Eocene–Miocene thrust activity in the Western Axial Zone and Chaînons Béarnais (west-central Pyrenees) revealed by multi-method thermochronology. *Comptes Rendus Geoscience*, *348*, 246–256. https://doi.org/10.1016/j.crte.2016.01.001

Boulvais, P. (2016). Fluid generation in the Boucheville Basin as a consequence of the North Pyrenean metamorphism. *Comptes Rendus Géosciences*, *348*, 301–311. https://doi.org/10.1016/j.crte.2015.06.013

Boulvais, P., de Parseval, P., D'Hulst, A., & Paris, P. (2006). Carbonate alteration associated with talc-chlorite mineralization in the eastern Pyrenees, with emphasis on the St. Barthelemy Massif. *Mineralogy and Petrology*, *88*, 499–526. https://doi.org/10.1007/s00710-006-0124-x

Boulvais, P., Ruffet, G., Cornichet, J., & Mermet, M. (2007). Cretaceous albitization and dequartzification of Hercynian peraluminous granite in the Salvezines Massif (French Pyrénées). *Lithos*, *93*(1-2), 89–106. https://doi.org/10.1016/j.lithos.2006.05.001

Bouquet, B. (1986). *La bordure mésozoïque orientale du Massif du Labourd (Pyrénées occidentales): Stratigraphie, sédimentologie, structure, implications géodynamiques* (Doctoral dissertation, p. 219). Pau: Université de Pau et des Pays de l'Adour.

Braun, J. (2009). Hot blanket in Earth's deep crust. *Nature*, *458*(7236), 292–293. https://doi.org/10.1038/458292a

Brune, S., Heine, C., Pérez-Gussinyé, M., & Sobolev, S. V. (2014). Rift migration explains continental margin asymmetry and crustal hyper-extension. *Nature Communications*, *5*, 4014. https://doi.org/10.1038/ncomms5014

Brune, S., Williams, S. E., Butterworth, N. P., & Müller, R. D. (2016). Abrupt plate accelerations shape rifted continental margins. *Nature*, *536*, 201–204. https://doi.org/10.1038/nature18319

Canérot, J. (1988). Manifestations de l'halocinèse dans les chaînons béarnais (zone Nord-Pyrénéenne) au Crétacé inférieur. *Comptes rendus de l'Académie des sciences. Série 2, Mécanique, Physique, Chimie, Sciences de l'univers, Sciences de la Terre*, *306*, 1099–1102.

Canérot, J. (1989). Rifting éocrétacé et halocinèse sur la marge ibérique des Pyrénées Occidentales (France). Conséquences structurales. *Bulletin des Centres de Recherches Exploration-Production Elf-Aquitaine*, *13*, 87–99.

Canérot, J. (2008). Les Pyrénées: Histoire géologique. Atlantica.

Canérot, J. (2018a). The pull apart-type Tardets-Mauléon Basin, a key to understand the formation of the Pyrenees. *Bulletin Société géologique de France*, *188*, 35.

Canérot, J. (2018b). Origine de la chaîne des Pyrénées: Collision entre les plaques ibérique et européenne ou inversion d'un ancien rift intracontinental avorté? *Bulletin de la Société d' Histoire Naturelle de Toulouse*, *153*, 95–110.

Canérot, J., Hudec, M. R., & Rockenbauch, K. (2005). Mesozoic diapirism in the Pyrenean orogen: Salt tectonics on a transform plate boundary. *AAPG Bulletin*, *89*(2), 211–229. https://doi.org/10.1306/09170404007

Casas, A., Kearey, P., Rivero, L., & Adam, C. R. (1997). Gravity anomaly map of the Pyrenean region and a comparison of the deep geological structure of the western and eastern Pyrenees. *Earth and Planetary Science Letters*, *150*(1–2), 65–78. https://doi.org/10.1016/S0012-821X(97)00087-3

Casas-Sainz, A. M., & Gil-Imaz, A. (1998). Extensional subsidence, contractional folding and thrust inversion of the eastern Cameros basin, northern Spain. *Geologische Rundschau*, *86*(4), 802–818. https://doi.org/10.1007/s005310050178

Casquet, C., Galindo, C., González-Casado, J. M., Alonso, A., Mas, R., Rodas, M., et al. (1992). El metamorfismo en la cuenca de los Cameros; geocronologia e implicaciones tectonicas. *Geogaceta*, *11*, 22–25.

Castañares, L. M., Robles, S., & Vicente Bravo, J. C. (1997). Distribución estratigráfica de los episodios volcánicos submarinos del Albiense-Santoniense en la Cuenca Vasca (sector Gernika-Plentzia, Bizkaia).

Casteras, M. (1933). Recherches sur la structure du versant nord des Pyrénées centrales et orientales. Libraire Polytechnique, C. Béranger.

Casteras, M., Gottis, M., Clin, M., Guignard, J., Paris, J., & Galharague, J. (1971). Carte géologique de la France au 1/50 000, feuille de Tardets–Sorholus, Orléans, France.

Casteras, M., Villanova, M., Godechot, J., Blanc, C., Labourguigne, J., Deloffre, R., et al. (1970). Carte géologique de la France au 1/50 000: feuille de Lourdes, Orléans, France.

Chelalou, R., Nalpas, T., Bousquet, R., Prevost, M., Lahfid, A., Poujol, M., et al. (2016). New sedimentological, structural and paleo-thermicity data in the Boucheville Basin (eastern North Pyrenean Zone, France). *Comptes Rendus Géoscience*, *348*, 312–321. https://doi.org/10.1016/j.crte.2015.11.008

Chevrot, S., Sylvander, M., Diaz, J., Martin, R., Mouthereau, F., Manatschal, G., et al. (2018). The non-cylindrical crustal architecture of the Pyrenees. *Scientific Reports*, *8*, 9591. https://doi.org/10.1038/s41598-018-27889-x

Choukroune, P. (1974). Structure et évolution tectonique de la zone nord-pyrénéenne: analyse de la déformation dans une portion de chaîne à schistosité sub-verticale.

Choukroune, P., & Etude Continentale et Océanique par Réflexion et réfraction Sismiques (ECORS) Team. (1989). The ECORS Pyrenean deep seismic profile reflection data and the overall structure of an orogenic belt. *Tectonics*, *8*(1), 23–39. https://doi.org/10.1029/TC008i001p00023

Choukroune, P., & Mattauer, M. (1978). Tectonique des plaques et Pyrénées; sur le fonctionnement de la faille transformante nord-pyrénéenne; comparaisons avec des modèles actuels. *Bulletin de la Société géologique de France*, *7*, 689–700. https://doi.org/10.2113/gssgfbull.s7-xx.5.689

Claude, D. (1990). *Etude stratigraphique, sédimentologique et structurale des dépôts mésozoïques au nord du massif du Labourd: Rôle de la faille de Pamplona* (Pays Basque) (Doctoral dissertation). Université de Bordeaux III.

Clauser, C., & Huenges, E. (1995). Thermal conductivity of rocks and minerals. In T. J. Ahrens (Ed.), *Rock physics and phase relations: A handbook of physical constants* (Vol. 3, pp. 105–126). Washington, DC: AGU.

Clerc, C. (2012). *Evolution du domaine nord-pyrénéen au Crétacé: amincissement crustal extrême et thermicité élevée: Un analogue pour les marges passives* (Doctoral dissertation). Paris 6.

Clerc, C., Boulvais, P., Lagabrielle, Y., & de Saint Blanquat, M. (2014). Ophicalcites from the northern Pyrenean belt: A field, petrographic and stable isotope study. *International Journal of Earth Sciences*, *103*, 141–163. https://doi.org/10.1007/s00531-013-0927-z

Clerc, C., & Lagabrielle, Y. (2014). Thermal control on the modes of crustal thinning leading to mantle exhumation: Insights from the Cretaceous Pyrenean hot paleomargins. *Tectonics*, *33*, 1340–1359. https://doi.org/10.1002/2013TC003471

Clerc, C., Lagabrielle, Y., Neumaier, M., Reynaud, J.-Y., & de Saint Blanquat, M. (2012). Exhumation of subcontinental mantle rocks: Evidence from ultramafic-bearing clastic deposits nearby the Lherz peridotite body, French Pyrenees. *Bulletin de la Société géologique de France*, *183*(5), 443–459. https://doi.org/10.2113/gssgfbull.183.5.443

Clerc, C., Lahfid, A., Monié, P., Lagabrielle, Y., Chopin, C., Poujol, M., et al. (2015). High-temperature metamorphism during extreme thinning of the continental crust: A reappraisal of the North Pyrenean passive paleomargin. *Solid Earth*, *6*(2), 643–668. https://doi.org/10.5194/se-6-643-2015

Combes, P.-J., Peybernès, B., & Leyreloup, A. F. (1998). Altérites et bauxites, témoins des marges européenne et ibérique des Pyrénées occidentales au Jurassique supérieur—Crétacé inférieur, à l'ouest de la vallée d'Ossau (Pyrénées-Atlantiques, France): Comptes Rendus de l'Académie des Sciences-Series II. *Earth and Planetary Science*, *327*(4), 271–278. https://doi.org/10.1016/s1251-8050(98)80085-2

Contrucci, I., Matias, L., Moulin, M., Géli, L., Klingelhofer, F., Nouzé, H., et al. (2004). Deep structure of the West African continental margin (Congo, Zaïre, Angola), between 5 S and 8 S, from reflection/refraction seismics and gravity data. *Geophysical Journal International*, *158*(2), 529–553. https://doi.org/10.1111/j.1365-246X.2004.02303.x

Corre, B. (2017). *La bordure nord de la plaque ibérique à l'Albo-Cénomanien: architecture d'une marge passive de type ductile (Chaînons Béarnais, Pyrénées Occidentales)* (Doctoral dissertation). Rennes 1.

Corre, B., Lagabrielle, Y., Labaume, P., Fourcade, S., Clerc, C., & Ballèvre, M. (2016). Deformation associated with mantle exhumation in a distal, hot passive margin environment: New constraints from the Saraillé Massif (Chaînons Béarnais, North-Pyrenean Zone). *Comptes Rendus Geoscience*, *348*, 279–289. https://doi.org/10.1016/j.crte.2015.11.007

Curnelle, R. (1983). Evolution structuro-sédimentaire du Trias et de l'Infra-Lias d'Aquitaine. *Bulletin des Centres de recherches exploration-production Elf-Aquitaine*, *7*(1), 69–99.

Daignières, M., Séguret, M., Specht, M., & Team ECORS (1994). The Arzacq-western Pyrenees ECORS deep seismic profile. In *Hydrocarbon and petroleum geology of France* (pp. 199–208). Berlin: Springer.

Dauteuil, O., & Ricou, L.-E. (1989). Une circulation de fluides de haute-température à l'origine du métamorphisme crétacé nord-pyrénéen. *Geodinamica Acta*, *3*(3), 237–249. https://doi.org/10.1080/09853111.1989.11105190

Debroas, E. J. (1978). Evolution de la fosse du flysch ardoisier de l'Albien superieur au Senonien inferieur (zone interne metamorphique des Pyrenees navarro-languedociennes). *Bulletin de la Société géologique de France*, *7*, 639–648.

Debroas, E. J. (1990). Le flysch noir albo-cenomanien temoin de la structuration albienne a senonienne de la Zone nord-pyreneenne en Bigorre (Hautes-Pyrenees, France). *Bulletin de la Societe Geologique de France*, *VI*(2), 273–285. https://doi.org/10.2113/gssgfbull.VI.2.273

Debroas, E.-J. (1987). Modèle de bassin triangulaire à l'intersection de décrochements divergents pour le fossé albo-cénomanien de la Ballongue (zone nord-pyrénéenne, France). *Bulletin de la Société géologique de France*, *III*(5), 887–898. https://doi.org/10.2113/gssgfbull.III.5.887

Debroas, E. J., Canérot, J., & Bilotte, M. (2010). Les brèches d'Urdach, témoins de l'exhumation du manteau pyrénéen dans un escarpement de faille vraconnien-cénomanien inférieur (Zone nord-pyrénéenne, Pyrénées-Atlantiques, France). *Géologie de la France.*, *2*, 53–63.

Decarlis, A., Manatschal, G., Haupert, I., & Masini, E. (2015). The tectono-stratigraphic evolution of distal, hyper-extended magma-poor conjugate rifted margins: Examples from the Alpine Tethys and Newfoundland–Iberia. *Marine and Petroleum Geology*, *68*, 54–72. https://doi.org/10.1016/j.marpetgeo.2015.08.005

Del Río, P., Barbero, L., Mata, P., & Fanning, C. M. (2009). Timing of diagenesis and very low-grade metamorphism in the eastern sector of the Sierra de Cameros (Iberian Range, Spain): A U-Pb SHRIMP study on monazite: U-Pb dating of diagenetic and low-grade monazite from the Iberian Range (Spain). *Terra Nova*, *21*(6), 438–445. https://doi.org/10.1111/j.1365-3121.2009.00900.x

Driscoll, N. W., Hogg, J. R., Christie-Blick, N., & Karner, G. D. (1995). Extensional tectonics in the Jeanne d'Arc Basin, offshore Newfoundland: Implications for the timing of break-up between Grand Banks and Iberia. *Geological Society of London, Special Publication*, *90*(1), 1–28. https://doi.org/10.1144/GSL.SP.1995.090.01.01

Dubois, P., & Seguin, J. C. (1978). Les flyschs cretace et eocene de la zone commingeoise et leur environnement. *Bulletin de la Societe Geologique de France*, *S7-XX*(5), 657–671. https://doi.org/10.2113/gssgfbull

Ducasse, L., & Vélasque, P.-C. (1988). *Géotraverse dans la partie occidentale des Pyrénées, de l'avant-pays aquitain au bassin de l'Ebre: effet d'une inversion structurale sur l'édification d'une chaîne intracontinentale* (Doctoral dissertation), Faculté des sciences et techniques de Saint-Jérôme, Université Paul Cézanne (Aix-Marseille).

Ducasse, L., Vélasque, P.-C., & Muller, J. (1986). Glissement de couverture et panneaux basculés dans la région des Arbailles (Pyrénées occidentales): Un modèle évolutif crétacé de la marge nord-ibérique à l'Est de la transformante de Pamplona. *Comptes rendus de l'Académie des sciences. Série 2, Mécanique, Physique, Chimie, Sciences de l'univers, Sciences de la Terre*, *303*, 1477–1482.

Ducoux, M. (2017). Structure, thermicité et évolution géodynamique de la Zone Interne Métamorphique des Pyrénées. Institut des Sciences de la Terre d'Orléans (ISTO).

Duée, G., Lagabrielle, Y., Coutelle, A., & Fortané, A. (1984). Les lherzolites associées aux Chaînons Béarnais (Pyrénées Occidentales): Mise à l'affleurement anté-dogger et resédimentation albo-cénomanienne. *Comptes-Rendus des Séances de l'Académie des Sciences. Série 2, Mécanique-Physique, Chimie, Sciences de l'univers, Sciences de la terre*, *299*, 1205–1210.

Duretz, T., Asti, R., Lagabrielle, Y., Brun, J., Jourdon, A., Clerc, C., & Corre, B. (2019). Numerical modelling of Cretaceous Pyrenean Rifting: The interaction between mantle exhumation and syn-rift salt tectonics. *Basin Research*, *38*(6), 1666. https://dx.doi.org/10.1111/bre.12389

Fabriès, J., Lorand, J.-P., & Bodinier, J.-L. (1998). Petrogenetic evolution of orogenic lherzolite massifs in the central and western Pyrenees. *Tectonophysics*, *292*(1-2), 145–167. https://doi.org/10.1016/S0040-1951(98)00055-9

Fabriès, J., Lorand, J.-P., Bodinier, J.-L., & Dupuy, C. (1991). Evolution of the upper mantle beneath the Pyrenees: Evidence from orogenic spinel lherzolite massifs. *Journal of Petrology*, *Special_Volume*(2), 55–76. https://doi.org/10.1093/petrology/Special_Volume.2.55

Fallourd, S., Poujol, M., Boulvais, P., Paquette, J.-L., de Saint Blanquat, M., & Rémy, P. (2014). In situ LA-ICP-MS U–Pb titanite dating of Na–Ca metasomatism in orogenic belts: The North Pyrenean example. *International Journal of Earth Sciences*, *103*, 667–682. https://doi.org/10.1007/s00531-013-0978-1

Ferralis, N., Matys, E. D., Knoll, A. H., Hallmann, C., & Summons, R. E. (2016). Rapid, direct and non-destructive assessment of fossil organic matter via micro-Raman spectroscopy. *Carbon*, *108*, 440–449. https://doi.org/10.1016/j.carbon.2016.07.039

Fixari, G. (1984). *Stratigraphie, faciès et dynamique tecto-sédimentaire du flysch albien (flysch noir et poudingues de Mendibelza) dans la région de Mauléon-Tardets (Pyrénées Atlantiques)* (Doctoral dissertation). Université Paul Sabatier de Toulouse (Sciences).

Ford, M., Hemmer, L., Vacherat, A., Gallagher, K., & Christophoul, F. (2016). Retro-wedge foreland basin evolution along the ECORS line, eastern Pyrenees, France. *Journal of the Geological Society*, *173*, 419–437. https://doi.org/10.1144/jgs2015-129

Fortané, A., Duée, G., Lagabrielle, Y., & Coutelle, A. (1986). Lherzolites and the western "Chaînons Béarnais" (French Pyrenees): Structural and paleogeographical pattern. *Tectonophysics*, *129*(1–4), 81–98. https://doi.org/10.1016/0040-1951(86)90247-7

Froitzheim, N., & Manatschal, G. (1996). Kinematics of Jurassic rifting, mantle exhumation, and passive-margin formation in the Austroalpine and Penninic nappes (eastern Switzerland). *Geological Society of America Bulletin*, *108*(9), 1120–1133. https://doi.org/10.1130/0016-7606(1996)108<1120:KOJRME>2.3.CO;2

Garcia-Senz, J., Pedrera, A., Ayala, C., Ruiz-Constán, A., Robador Moreno, A., & Rodríguez-Fernández, R. (2019). *Inversion of the North-Iberian hyperextended margin: The role of exhumed mantle indentation during continental collision* (Geological Society, London, Special Publications, SP490-2019-112). https://doi.org/10.1144/SP490-2019-112

Golberg, J. M., Guiraud, M., Maluski, H., & Séguret, M. (1988). Caractères pétrologiques et âge du métamorphisme en contexte distensif du bassin sur décrochement de Soria (Crétacé inférieur, Nord Espagne). *Comptes rendus de l'Académie des sciences. Série 2, Mécanique, Physique, Chimie, Sciences de l'univers, Sciences de la Terre*, *307*, 521–527.

Golberg, J. M., & Leyreloup, A. F. (1990). High temperature-low pressure Cretaceous metamorphism related to crustal thinning (Eastern North Pyrenean Zone, France). *Contributions to Mineralogy and Petrology*, *104*(2), 194–207. https://doi.org/10.1007/BF00306443

Golberg, J.-M., & Maluski, H. (1988). Données nouvelles et mise au point sur l'âge du métamorphisme pyrénéen. *Comptes rendus de l'Académie des sciences. Série 2, Mécanique, Physique, Chimie, Sciences de l'univers, Sciences de la Terre*, *306*, 429–435.

Golberg, J. M., Maluski, H., & Leyreloup, A. F. (1986). Petrological and age relationship between emplacement of magmatic breccia, alkaline magmatism, and static metamorphism in the North Pyrenean Zone. *Tectonophysics*, *129*(1–4), 275–290. https://doi.org/10.1016/0040-1951(86)90256-8

Gottis, M. (1972). Construction d'un modèle géodynamique pyrénéen. *Comptes Rendus. Académie des Sciences*, *275*, 2099.

Grandjean, G. (1992). *Mise en évidence des structures crustales dans une portion de chaîne et de leur relation avec les bassins sédimentaires. Application aux Pyrénées occidentales au travers du Projet ECORS Arzacq-Pyrénées* (Doctoral dissertation). Université des Sciences et Techniques du Languedoc.

Grandjean, G. (1994). Etude des structures crustales dans une portion de chaîne et de leur relation avec les bassins sédimentaires. Application aux Pyrénées occidentales. *Bulletin des Centres de Recherches Exploration-Production Elf-Aquitaine*, *18*, 391–420.

Grigné, C., Labrosse, S., & Tackley, P. J. (2007). Convection under a lid of finite conductivity: Heat flux scaling and application to continents. *Journal of Geophysical Research*, *112*, B08402. https://doi.org/10.1029/2005JB004192

Grool, A. R., Ford, M., Vergés, J., Huismans, R. S., Christophoul, F., & Dielforder, A. (2018). Insights into the crustal-scale dynamics of a doubly vergent orogen from a quantitative analysis of its forelands: A case study of the eastern Pyrenees. *Tectonics*, *37*, 450–476. https://doi.org/10.1002/2017TC004731

Guedes, A., Valentim, B., Prieto, A. C., Rodrigues, S., & Noronha, F. (2010). Micro-Raman spectroscopy of collotelinite, fusinite and macrinite. *International Journal of Coal Geology*, *83*(4), 415–422. https://doi.org/10.1016/j.coal.2010.06.002

Guillou, L., & Jaupart, C. (1995). On the effect of continents on mantle convection. *Journal of Geophysical Research*, *100*(B12), 24,217–24,238. https://doi.org/10.1029/95JB02518

Guillou-Frottier, L., Carré, C., Bourgine, B., Bouchot, V., & Genter, A. (2013). Structure of hydrothermal convection in the Upper Rhine Graben as inferred from corrected temperature data and basin-scale numerical models. *Journal of Volcanology and Geothermal Research*, *256*, 29–49. https://doi.org/10.1016/j.jvolgeores.2013.02.008

Guillou-Frottier, L., Lucazeau, F., Garibaldi, C., Bonté, D., & Coueffé, R. (2010). Heat flow and deep temperatures in the Southeast Basin of France: Implications for local rheological contrasts. *Bulletin de la Société Géologique de France*, *181*(6), 531–546. https://doi.org/10.2113/gssgfbull.181.6.531

Guiraud, M., & Séguret, M. (1985). A releasing solitary overstep model for the Late Jurassic-Early Cretaceous (Wealdian) Soria strike-slip basin (northern Spain). AAPG Bull.

Handy, M. R., Schmid, S. M., Bousquet, R., Kissling, E., & Bernoulli, D. (2010). Reconciling plate-tectonic reconstructions of Alpine Tethys with the geological–geophysical record of spreading and subduction in the Alps. *Earth Science Reviews*, *102*(3–4), 121–158. https://doi.org/10.1016/j.earscirev.2010.06.002

Hart, N. R., Stockli, D. F., Lavier, L. L., & Hayman, N. W. (2017). Thermal evolution of a hyperextended rift basin, Mauléon Basin, western Pyrenees: Thermal evolution of hyperextended rift. *Tectonics*, *36*, 1103–1128. https://doi.org/10.1002/2016TC004365

Haupert, I., Manatschal, G., Decarlis, A., & Unternehr, P. (2016). Upper-plate magma-poor rifted margins: Stratigraphic architecture and structural evolution. *Marine and Petroleum Geology*, *69*, 241–261. https://doi.org/10.1016/j.marpetgeo.2015.10.020

Henry, D. G., Jarvis, I., Gillmore, G., & Stephenson, M. (2019). Raman spectroscopy as a tool to determine the thermal maturity of organic matter: Application to sedimentary, metamorphic and structural geology. *Earth-Science Reviews*, *198*, 102936. https://doi.org/10.1016/j.earscirev.2019.102936

Henry, D. G., Jarvis, I., Gillmore, G., Stephenson, M., & Emmings, J. (2018). Assessing low maturity organic matter in shales using Raman spectroscopy: Effects of sample preparation and operating procedure. *International Journal of Coal Geology*, *191*, 135–151. https://doi.org/10.1016/j.coal.2018.03.005

Henry, P., Azambre, B., Montigny, R., Rossy, M., & Stevenson, R. K. (1998). Late mantle evolution of the Pyrenean sub-continental lithospheric mantle in the light of new ^{40}Ar–^{39}Ar and Sm–Nd ages on pyroxenites and peridotites (Pyrenees, France). *Tectonophysics*, *296*(1–2), 103–123. https://doi.org/10.1016/S0040-1951(98)00139-5

Hinrichs, R., Brown, M. T., Vasconcellos, M. A. Z., Abrashev, M. V., & Kalkreuth, W. (2014). Simple procedure for an estimation of the coal rank using micro-Raman spectroscopy. *International Journal of Coal Geology*, *136*, 52–58. https://doi.org/10.1016/j.coal.2014.10.013

Huismans, R. S., & Beaumont, C. (2003). Symmetric and asymmetric lithospheric extension: Relative effects of frictional-plastic and viscous strain softening. *Journal of Geophysical Researché- Solid Earth*, *108*(B10), 2496. https://doi.org/10.1029/2002JB002026

Huismans, R. S., & Beaumont, C. (2008). Complex rifted continental margins explained by dynamical models of depth-dependent lithospheric extension. *Geology*, *36*(2), 163. https://doi.org/10.1130/G24231A.1

Huismans, R. S., & Beaumont, C. (2011). Depth-dependent extension, two-stage breakup and cratonic underplating at rifted margins. *Nature*, *473*(7345), 74–78. https://doi.org/10.1038/nature09988

Huismans, R. S., & Beaumont, C. (2014). Rifted continental margins: The case for depth-dependent extension. *Earth and Planetary Science Letters*, *407*, 148–162. https://doi.org/10.1016/j.epsl.2014.09.032

Issautier, B., Saspiturry, N., & Serrano, O. (2020). Structural inheritance and salt tectonics controlling pseudosymmetric rift formation during Early Cretaceous hyperextension of the Arzacq and Tartas Basins (southwest France). *Marine and Petroleum Geology*, *118*, 104395. https://doi.org/10.1016/j.marpetgeo.2020.104395

Jammes, S., Manatschal, G., Lavier, L., & Masini, E. (2009). Tectono-sedimentary evolution related to extreme crustal thinning ahead of a propagating ocean: Example of the western Pyrenees. *Tectonics*, *28*, TC4012. https://doi.org/10.1029/2008TC002406

Jaupart, C., & Mareschal, J.-C. (2007). Heat flow and thermal structure of the lithosphere. In A. B. Watts (Ed.), *Crustal and Lithosphere Dynamics*, *Treatise on Geophysics* (Vol. 6, pp. 217–251). New York: Elsevier.Jaupart, C., & Mareschal, J.-C. (2011). *Heat generation and transport in the Earth* (p. 464). Amsterdam: Cambridge University Press.

Jehlička, J., Urban, O., & Pokorny, J. (2003). Raman spectroscopy of carbon and solid bitumens in sedimentary and metamorphic rocks. *Spectrochimica Acta. Part A, Molecular and Biomolecular Spectroscopy*, *59*(10), 2341–2352. https://doi.org/10.1016/S1386-1425(03)00077-5

Jourdon, A., Mouthereau, F., Pourhiet, L., & Callot, J. (2020). Topographic and tectonic evolution of mountain belts controlled by salt thickness and rift architecture. *Tectonics*, *39*, e2019TC005903. https://dx.doi.org/10.1029/2019tc005903

Jourdon, A., Pourhiet, L., Mouthereau, F., & Masini, E. (2019). Role of rift maturity on the architecture and shortening distribution in mountain belts. *Earth and Planetary Science Letters*, *512*, 89–99. https://dx.doi.org/10.1016/j.epsl.2019.01.057

Karner, G. D., Driscoll, N. W., & Barker, D. H. N. (2003). Syn-rift regional subsidence across the West African continental margin: The role of lower plate ductile extension. *Geological Society of London, Special Publication*, *207*(1), 105–129. https://doi.org/10.1144/GSL.SP.2003.207.6

Karner, G. D., & Gambôa, L. A. P. (2007). Timing and origin of the South Atlantic pre-salt sag basins and their capping evaporites. *Geological Society of London, Special Publication*, *285*, 15–35. https://doi.org/10.1144/SP285.2

Kodaira, S., Mjelde, R., Gunnarsson, K., Shiobara, H., & Shimamura, H. (1998). Structure of the Jan Mayen microcontinent and implications for its evolution. *Geophysical Journal International*, *132*(2), 383–400. https://doi.org/10.1046/j.1365-246x.1998.00444.x

Labaume, P., Meresse, F., Jolivet, M., & Teixell, A. (2016). Exhumation sequence of the basement thrust units in the west-central Pyrenees. Constraints from apatite fission track analysis. *Geogaceta*, *60*, 11–14.

Labaume, P., Séguret, M., & Seyve, C. (1985). Evolution of a turbiditic foreland basin and analogy with an accretionary prism: Example of the Eocene South-Pyrenean basin. *Tectonics*, *4*(7), 661–685. https://doi.org/10.1029/TC004i007p00661

Labaume, P., & Teixell, A. (2020). Evolution of salt structures of the Pyrenean rift (Chaînons Béarnais, France): From hyper-extension to tectonic inversion. *Tectonophysics*, *785*, 228451. https://doi.org/10.1016/j.tecto.2020.228451

Lagabrielle, Y., Asti, R., Duretz, T., Clerc, C., Fourcade, S., Teixell, A., & Saspiturry, N. (2020). A review of cretaceous smooth-slopes extensional basins along the Iberia-Eurasia plate boundary: How pre-rift salt controls the modes of continental rifting and mantle exhumation. *Earth-Science Reviews*, *190*(1). https://doi.org/10.1051/bsgf/2019007

Lagabrielle, Y., & Bodinier, J.-L. (2008). Submarine reworking of exhumed sub-continental mantle rocks: Field evidence from the Lherz peridotites, French Pyrenees: Cretaceous exhumation of Pyrenean mantle. *Terra Nova*, *20*, 11–21. https://doi.org/10.1111/j.1365-3121.2007.00781.x

Lagabrielle, Y., Clerc, C., Vauchez, A., Lahfid, A., Labaume, P., Azambre, B., et al. (2016). Very high geothermal gradient during mantle exhumation recorded in mylonitic marbles and carbonate breccias from a Mesozoic Pyrenean palaeomargin (Lherz area, North Pyrenean Zone, France). *Comptes Rendus Geoscience*, *348*, 290–300. https://doi.org/10.1016/j.crte.2015.11.004

Lagabrielle, Y., Labaume, P., & de Saint Blanquat, M. (2010). Mantle exhumation, crustal denudation, and gravity tectonics during Cretaceous rifting in the Pyrenean realm (SW Europe): Insights from the geological setting of the lherzolite bodies. *Tectonics*, *29*, TC4012. https://doi.org/10.1029/2009TC002588

Lahfid, A., Baidder, L., Ouanaimi, H., Soulaimani, A., Hoepffner, C., Farah, A., et al. (2019). From extension to compression: High geothermal gradient during the earliest Variscan phase of the Moroccan Meseta; a first structural and RSCM thermometric study. *European Journal of Mineralogy*, *31*(4), 695–713. https://doi.org/10.1127/ejm/2019/0031-2882

Lahfid, A., Beyssac, O., Deville, E., Negro, F., & Goffé, B. (2010). Evolution of the Raman spectrum of carbonaceous material in low-grade metasediments of the Glarus Alps (Switzerland). *Terra Nova*, *22*, 354–360. https://doi.org/10.1111/j.1365-3121.2010.00956.x

Lamare, P. (1936). *Recherches géologiques dans les Pyrénées basques d'Espagne*. Société géologique de France.

Lamolda, M., Mathey, B., Rossy, M., & Sigal, J. (1983). La edad del volcanismo cretácico de Vizcaya y Guipuzcoa. *Estudios Geológicos*, *39*, 151–156.

Lavier, L. L., & Manatschal, G. (2006). A mechanism to thin the continental lithosphere at magma-poor margins. *Nature*, *440*(7082), 324–328. https://doi.org/10.1038/nature04608

Lemoine, M., Tricart, P., & Boillot, G. (1987). Ultramafic and gabbroic ocean floor of the Ligurian Tethys (Alps, Corsica, Apennines): In search of a genetic model. *Geology*, *15*(7), 622–625. https://doi.org/10.1130/0091-7613(1987)15<622:UAGOFO>2.0.CO;2

Lenoble, J.-L. (1992). *Les plates-formes carbonatées ouest-pyrénéennes du dogger à l'Albien, stratigraphie séquentielle et évolution géodynamique* (Doctoral dissertation). Université Paul Sabatier de Toulouse (Sciences).

Lescoutre, R., Tugend, J., Brune, S., Masini, E., & Manatschal, G. (2019). Thermal evolution of asymmetric hyperextended magma-poor rift systems: Results from numerical modeling and Pyrenean field observations. *Geochemistry, Geophysics, Geosystems*, *20*, e2019GC008600. https://doi.org/10.1029/2019GC008600

López-Horgue, M. A., Owen, H. G., Rodríguez-Lázaro, J., Fernández-Mendiola, P. A., & García-Mondéjar, J. (1999). Late Albian–Early Cenomanian stratigraphic succession near Estella-Lizarra (Navarra, central northern Spain) and its regional and interregional correlation. *Cretaceous Research*, *20*(4), 369–402. https://doi.org/10.1006/cres.1999.0162

Lucas, C. (1985). *Le grès rouge du versant nord des Pyrénées: essai sur la géodynamique de dépôts continentaux du permien et du trias* (p. 267).

Lucazeau, F., Leroy, S., Rolandone, F., d'Acremont, E., Watremez, L., Bonneville, A., et al. (2010). Heat-flow and hydrothermal circulation at the ocean–continent transition of the eastern Gulf of Aden. *Earth and Planetary Science Letters*, *295*(3-4), 554–570. https://doi.org/10.1016/j.epsl.2010.04.039

Lunsdorf, N. K., Dunkl, I., Schmidt, B. C., Rantitsch, G., & von Eynatten, H. (2017). Towards a higher comparability of geothermometric data obtained by Raman spectroscopy of carbonaceous material. Part 2: A revised geothermometer. *Geostandards and Geoanalytical Research*, *41*, 593–612. https://doi.org/10.1111/ggr.12178

Macchiavelli, C., Vergés, J., Schettino, A., Fernàndez, M., Turco, E., Casciello, E., et al. (2017). A new southern North Atlantic isochron map: Insights into the drift of the Iberian plate since the Late Cretaceous: Iberian Plate Kinematics Since 83.5 Ma. *Journal of Geophysical Research: Solid Earth*, *122*, 9603–9626. https://doi.org/10.1002/2017JB014769

Magri, F., Inbar, N., Siebert, C., Rosenthal, E., Guttman, J., & Möller, P. (2015). Transient simulations of large-scale hydrogeological processes causing temperature and salinity anomalies in the Tiberias Basin. *Journal of Hydrology*, *520*, 342–355. https://doi.org/10.1016/j.jhydrol.2014.11.055

Magri, F., Littke, R., Rodon, S., & Urai, J. L. (2008). Temperature fields, petroleum maturation and fluid flow in the vicinity of salt domes. In R. Littke, U. Bayer, D. Gajewski, S. Nelskamp (Eds.), *Dynamics of Complex Intracontinental Basins: The Central European Basin System* (pp. 323–344). Berlin-Heidelberg: Springer.

Manatschal, G., Engström, A., Desmurs, L., Schaltegger, U., Cosca, M., Müntener, O., & Bernoulli, D. (2006). What is the tectono-metamorphic evolution of continental break-up: The example of the Tasna Ocean–Continent Transition. *Journal of Structural Geology*, *28*(10), 1849–1869. https://doi.org/10.1016/j.jsg.2006.07.014

Manatschal, G., Froitzheim, N., Rubenach, M., & Turrin, B. D. (2001). The role of detachment faulting in the formation of an ocean-continent transition: Insights from the Iberia Abyssal Plain. *Geological Society of London, Special Publication*, *187*(1), 405–428. https://doi.org/10.1144/GSL.SP.2001.187.01.20

Manatschal, G., Marquer, D., & Früh-Green, G. L. (2000). Channelized fluid flow and mass transfer along a rift-related detachment fault (Eastern Alps, southeast Switzerland). *Geological Society of America Bulletin*, *112*(1), 21–33. https://doi.org/10.1130/0016-7606(2000)112<21:CFFAMT>2.0.CO;2

Manatschal, G., & Nievergelt, P. (1997). A continent-ocean transition recorded in the Err and Platta nappes (Eastern Switzerland). *Eclogae Geologicae Helvetiae*, *90*, 3–28.

Manatschal, G., Sauter, D., Karpoff, A. M., Masini, E., Mohn, G., & Lagabrielle, Y. (2011). The Chenaillet Ophiolite in the French/Italian Alps: An ancient analogue for an Oceanic Core Complex? *Lithos, Alpine Ophiolites and Modern AnaloguesContinental Rifting to Oceanic Lithosphere Alpine Ophiolites and Modern Analogues*, *124*(3-4), 169–184. https://doi.org/10.1016/j.lithos.2010.10.017

Marques, M., Suarez-Ruiz, I., Flores, D., Guede, A., & Rodrigues, S. (2009). Correlation between optical, chemical and micro-structural parameters of high-rank coals and graphite. *International Journal of Coal Geology*, *77*, 377–382. https://doi.org/10.1016/j.coal.2008.06.002

Martínez-Torres, L. M. (1989). *El manto de los mármoles (Pirineo occidental): Geología estructural y evolución geodinámica* (Doctoral dissertation). Universidad del País Vasco-Euskal Herriko Unibertsitatea.

Masini, E., Manatschal, G., & Mohn, G. (2013). The Alpine Tethys rifted margins: Reconciling old and new ideas to understand the stratigraphic architecture of magma-poor rifted margins. *Sedimentology*, *60*, 174–196. https://doi.org/10.1111/sed.12017

Masini, E., Manatschal, G., Mohn, G., Ghienne, J.-F., & Lafont, F. (2011). The tectono-sedimentary evolution of a supra-detachment rift basin at a deep-water magma-poor rifted margin: The example of the Samedan Basin preserved in the Err nappe in SE Switzerland: Tectono-sedimentary evolution of a supra-detachment rift basin. *Basin Research*, *23*(6), 652–677. https://doi.org/10.1111/j.1365-2117.2011.00509.x

Masini, E., Manatschal, G., Tugend, J., Mohn, G., & Flament, J.-M. (2014). The tectono-sedimentary evolution of a hyper-extended rift basin: The example of the Arzacq–Mauléon rift system (Western Pyrenees, SW France). *International Journal of Earth Sciences*, *103*, 1569–1596. https://doi.org/10.1007/s00531-014-1023-8

Mata, M. P., Casas, A. M., Canals, A., Gil, A., & Pocovi, A. (2001). Thermal history during Mesozoic extension and Tertiary uplift in the Cameros Basin, northern Spain. *Basin Research*, *13*(1), 91–111. https://doi.org/10.1046/j.1365-2117.2001.00138.x

Mattauer, M. (1968). Les traits structuraux essentiels de la chaîne Pyrénéenne. *Revue de Geologie Dynamique et de Geographie Physique*, *10*, 3–11.

Mello, U. T., Karner, G. D., & Anderson, R. N. (1995). Role of salt in restraining the maturation of subsalt source rocks. *Marine and Petroleum Geology*, *12*(7), 697–716. https://doi.org/10.1016/0264-8172(95)93596-V

Mendia, M. S., & Ibarguchi, J. I. G. (1991). High-grade metamorphic rocks and peridotites along the Leiza Fault (Western Pyrenees, Spain). *Geologische Rundschau*, *80*(1), 93–107. https://doi.org/10.1007/BF01828769

Mjelde, R., Digranes, P., Van Schaack, M., Shimamura, H., Shiobara, H., Kodaira, S., et al. (2001). Crustal structure of the outer Vøring Plateau, offshore Norway, from ocean bottom seismic and gravity data. *Journal of Geophysical Research*, *106*(B4), 6769–6791. https://doi.org/10.1029/2000JB900415

Mjelde, R., Raum, T., Breivik, A. J., & Faleide, J. I. (2008). Crustal transect across the North Atlantic. *Marine Geophysical Researches*, *29*, 73–87. https://doi.org/10.1007/s11001-008-9046-9

Mohn, G., Manatschal, G., Beltrando, M., Masini, E., & Kusznir, N. (2012). Necking of continental crust in magma-poor rifted margins: Evidence from the fossil Alpine Tethys margins: Necking of continental crust. *Tectonics*, *31*, TC1012. https://doi.org/10.1029/2011TC002961

Moine, B., Fortune, J. P., Moreau, P., & Viguier, F. (1989). Comparative mineralogy, geochemistry, and conditions of formation of two metasomatic talc and chlorite deposits; Trimouns (Pyrenees, France) and Rabenwald (Eastern Alps, Austria). *Economic Geology*, *84*(5), 1398–1416. https://doi.org/10.2113/gsecongeo.84.5.1398

Montigny, R., Azambre, B., Rossy, M., & Thuizat, R. (1986). K-Ar study of Cretaceous magmatism and metamorphism in the Pyrenees: Age and length of rotation of the Iberian Peninsula. *Tectonophysics, The Geological Evolution of the Pyrenees*, *129*(1–4), 257–273. https://doi.org/10.1016/0040-1951(86)90255-6

Moulin, M., Aslanian, D., Olivet, J.-L., Contrucci, I., Matias, L., Géli, L., et al. (2005). Geological constraints on the evolution of the Angolan margin based on reflection and refraction seismic data (ZaïAngo project). *Geophysical Journal International*, *162*(3), 793–810. https://doi.org/10.1111/j.1365-246X.2005.02668.x

Moulin, M., Aslanian, D., & Unternehr, P. (2010). A new starting point for the South and Equatorial Atlantic Ocean. *Earth Science Reviews*, *98*(1–2), 1–37. https://doi.org/10.1016/j.earscirev.2009.08.001

Mouthereau, F., Filleaudeau, P.-Y., Vacherat, A., Pik, R., Lacombe, O., Fellin, M. G., et al. (2014). Placing limits to shortening evolution in the Pyrenees: Role of margin architecture and implications for the Iberia/Europe convergence. *Tectonics*, *33*, 2283–2314. https://doi.org/10.1002/2014TC003663

Muller, J., & Roger, P. (1977). L'Evolution structurale des Pyrénées (Domaine central et occidental) Le segment hercynien, la chaîne de fond alpine. *Géologie Alpine*, *53*, 149–191.

Muñoz, J. A. (1992). Evolution of a continental collision belt: ECORS-Pyrenees crustal balanced cross-section. In K. R. McClay (Ed.), *Thrust Tectonics* (pp. 235–246). Netherlands: Springer. https://doi.org/10.1007/978-94-011-3066-0_21

Muraoka, H., Yasukawa, K., & Kimbara, K. (2000). *Current state of development of deep geothermal resources in the world and implications to the future* (pp. 1479–1484). Paper presented at Proceedings World Geothemal Congress, Kyushu-Tohoku, Japan.

Nábělek, P. I., & Nábělek, J. L. (2014). Thermal characteristics of the Main Himalaya Thrust and the Indian lower crust with implications for crustal rheology and partial melting in the Himalaya orogen. *Earth and Planetary Science Letters*, *395*, 116–123. https://doi.org/10.1016/j.epsl.2014.03.026

Nirrengarten, M., Mohn, G., Schito, A., Corrado, S., Gutiérrez-García, L., Bowden, S. A., & Despinois, F. (2019). The thermal imprint of continental breakup during the formation of the South China Sea. *Earth and Planetary Science Letters*, *531*, 115972. https://doi.org/10.1016/j.epsl.2019.115972

Omodeo-Salé, S., Salas, R., Guimerà, J., Ondrak, R., Mas, R., Arribas, J., et al. (2017). Subsidence and thermal history of an inverted Late Jurassic-Early Cretaceous extensional basin (Cameros, North-central Spain) affected by very low- to low-grade metamorphism. *Basin Research*, *29*, 156–174. https://doi.org/10.1111/bre.12142

Ortiz, A. (2019). *Géométries et bilan érosion-sédimentation d'un rétro-bassin d'avant-pays durant son évolution finie-orogénique et post-orogénique: Le cas du système Pyrénées/bassin d'Aquitaine/golfe de Gascogne de 38 à 0 Ma* (PhD thesis, p. 386). Université de Rennes 1.

Ortiz, A., Guillocheau, F., Lasseur, E., Briais, J., Robin, C., Serrano, O., & Fillon, C. (2019). Sediment routing system and sink preservation during the post-orogenic evolution of a retro-foreland basin: The case example of the North Pyrenean (Aquitaine, Bay of Biscay) Basins. *Marine and Petroleum Geology*, *112*, 104085. https://doi.org/10.1016/j.marpetgeo.2019.104085

Pérez-Gussinyé, M. (2013). A tectonic model for hyperextension at magma-poor rifted margins: An example from the West Iberia–Newfoundland conjugate margins. *Geological Society of London, Special Publication*, *369*, 403–427. https://doi.org/10.1144/SP369.19

Péron-Pinvidic, G., Gernigon, L., Gaina, C., & Ball, P. (2012a). Insights from the Jan Mayen system in the Norwegian–Greenland Sea—I. Mapping of a microcontinent. *Geophysical Journal International*, *191*(2), 385–412. https://doi.org/10.1111/j.1365-246X.2012.05639.x

Péron-Pinvidic, G., Gernigon, L., Gaina, C., & Ball, P. (2012b). Insights from the Jan Mayen system in the Norwegian–Greenland Sea—II. Architecture of a microcontinent. *Geophysical Journal International*, *191*(2), 413–435. https://doi.org/10.1111/j.1365-246X.2012.05623.x

Péron-Pinvidic, G., & Manatschal, G. (2009). The final rifting evolution at deep magma-poor passive margins from Iberia-Newfoundland: A new point of view. *International Journal of Earth Sciences*, *98*, 1581–1597. https://doi.org/10.1007/s00531-008-0337-9

Péron-Pinvidic, G., Manatschal, G., Masini, E., Sutra, E., Flament, J. M., Haupert, I., & Unternehr, P. (2015). Unravelling the along-strike variability of the Angola–Gabon rifted margin: A mapping approach. *Geological Society of London, Special Publication*, *438*, 49–76. https://doi.org/10.1144/SP438.1

Péron-Pinvidic, G., Manatschal, G., Minshull, T. A., & Sawyer, D. S. (2007). Tectonosedimentary evolution of the deep Iberia-Newfoundland margins: Evidence for a complex breakup history. *Tectonics*, *26*, TC2011. https://doi.org/10.1029/2006TC001970

Peron-Pinvidic, G., Manatschal, G., & Osmundsen, P. T. (2013). Structural comparison of archetypal Atlantic rifted margins: A review of observations and concepts. *Marine and Petroleum Geology*, *43*, 21–47. https://doi.org/10.1016/j.marpetgeo.2013.02.002

Poujol, M., Boulvais, P., & Kosler, J. (2010). Regional-scale Cretaceous albitization in the Pyrenees: Evidence from in situ U–Th–Pb dating of monazite, titanite and zircon. *Journal of the Geological Society*, *167*(4), 751–767. https://doi.org/10.1144/0016-76492009-144

Rat, J., Mouthereau, F., Brichau, S., Crémades, A., Bernet, M., Balvay, M., et al. (2019). Tectonothermal evolution of the Cameros basin: Implications for tectonics of North Iberia. *Tectonics*, *38*, 440–469. https://doi.org/10.1029/2018TC005294

Rat, P. (1959). *Les pays crétacés: Basco-cantabriques (Espagne)*. Dijon: Presses universitaires de France.

Rat, P., Amiot, M., Feuillée, P., Floquet, M., Mathey, B., Pascal, A., et al. (1983). Vue sur le Cretacé basco-cantabrique et nord-ibérique. Une Marge Son Arriere-Pays Ses Environ. Sedimentaires Memoires Geol. Univ. Dijon 9, 191.

Ravier, J. (1957). *Le métamorphisme des terrains secondaires des Pyrénées* (Doctoral dissertation). Université, Faculté des Sciences.

Razin, P. (1989). *Evolution tecto-sédimentaire alpine des Pyrénées basques à l'ouest de la transformante de Pamplona, Province du Labourd* (Doctoral dissertation). Bordeaux 3.

Rebelo, S. L. H., Guedes, A., Szefczyk, M. E., Pereira, A. M., Araújo, J. P., & Freire, C. (2016). Progress in the Raman spectra analysis of covalently functionalized multiwalled carbon nanotubes: unraveling disorder in graphitic materials. *Physical Chemistry Chemical Physics*, *18*, 12,784–12,796. https://doi.org/10.1039/C5CP06519D

Reston, T. (2007). Extension discrepancy at North Atlantic non-volcanic rifted margins: Depth-dependent stretching or unrecognized faulting? *Geology*, *35*(4), 367–370. https://doi.org/10.1130/G23213A.1

Reston, T. J. (2009). The structure, evolution and symmetry of the magma-poor rifted margins of the North and Central Atlantic: A synthesis. *Tectonophysics*, *468*, 6–27. https://doi.org/10.1016/j.tecto.2008.09.002

Roche, V., Sternai, P., Guillou-Frottier, L., Menant, A., Jolivet, L., Bouchot, V., & Gerya, T. (2018). Emplacement of metamorphic core complexes and associated geothermal systems controlled by slab dynamics. *Earth and Planetary Science Letters*, *498*, 322–333. https://doi.org/10.1016/j.epsl.2018.06.043

Rossy, M., Azambre, B., & Albarède, F. (1992). REE and Sr/1bNd isotope geochemistry of the alkaline magmatism from the Cretaceous North Pyrenean Rift Zone (France-Spain). *Chemical Geology*, *97*(1–2), 33–46. https://doi.org/10.1016/0009-2541(92)90134-Q

Roux, J.-C. (1983). *Recherches stratigraphiques et sédimentologiques sur les flyschs crétacés pyrénéens au sud d'Oloron (Pyrénées Atlantiques)* (Doctoral dissertation). Université Paul Sabatier de Toulouse (Sciences).

Rubatto, D., Gebauer, D., & Fanning, M. (1998). Jurassic formation and Eocene subduction of the Zermatt-Saas-Fee ophiolites: Implications for the geodynamic evolution of the Central and Western Alps. *Contributions to Mineralogy and Petrology*, *132*(3), 269–287. https://doi.org/10.1007/s004100050421

Sadezky, A., Muckenhuber, H., Grothe, R., Niessner, G., & Pöschl, U. (2005). Raman microspectroscopy of soot and related carbonaceous materials: Spectral analysis and structural information. *Carbon*, *43*, 1731–1742. https://doi.org/10.1016/j.carbon.2005.02.018

Saspiturry, N. (2019). *Evolution sédimentaire, structurale et thermique d'un rift hyper-aminci: de l'héritage post-hercynien à l'inversion alpine, Exemple du bassin de Mauléon (Pyrénées)* (PhD thesis, p. 444). Bordeaux University.

Saspiturry, N., Allanic, C., Razin, P., Issautier, B., Baudin, T., Lasseur, E., & Leleu, S. (2020). Closure of a hyperextended system in an orogenic lithospheric pop-up, Western Pyrenees: The role of mantle buttressing and rift structural inheritance. *Terra Nova*, *32*(4), 253–260. https://doi.org/10.1111/ter.12457

Saspiturry, N., Cochelin, B., Razin, P., Leleu, S., Lemirre, B., Bouscary, B., et al. (2019). Tectono-sedimentary evolution of a rift-system controlled by Permian post-orogenic extension and MCC formation (Bidarray Basin and Ursuya dome, Western Pyrenees). *Tectonophysics*, *768*, 228180. https://doi.org/10.1016/j.tecto.2019.228180

Saspiturry, N., Lahfid, A., Baudin, T., Guillou-Frottier, G., Razin, P., Issautier, B., et al. (2020). *N Saspiturry Mauléon basin. RSCM peak temperatures, Mendeley Data, V3*. https://doi.org/10.17632/47kgv7r9wm.2

Saspiturry, N., Razin, P., Baudin, T., Serrano, O., Issautier, B., Lasseur, E., et al. (2019). Symmetry vs. asymmetry of a hyper-thinned rift: Example of the Mauléon Basin (Western Pyrenees, France). *Marine and Petroleum Geology*, *104*, 86–105. https://doi.org/10.1016/j.marpetgeo.2019.03.031

Schito, A., & Corrado, S. (2018). An automatic approach for characterization of the thermal maturity of dispersed organic matter Raman spectra at low diagenetic stages. In P. Dowey, M. Osborne, H. Volk (Eds.), *Application of analytical techniques to petroleum systems* (pp. 125–138). London: Geological Society, London, Special Publications. https://doi.org/10.1144/SP484.5 SP484.5

Schito, A., Romano, C., Corrado, S., Grigo, D., Poe, B. (2017). Diagenetic thermal evolution of organic matter by Raman spectroscopy. *Organic Geochemistry*, *106*, 57–67. https://doi.org/10.1016/j.orggeochem.2016.12.006

Schmidt, J. L., Hinrichs, R., & Araujo, C. V. (2017). Maturity estimation of phytoclasts in strew mounts by micro-Raman spectroscopy. *International Journal of Coal Geology*, *173*, 1–8. https://doi.org/10.1016/j.coal.2017.02.003

Schoeffler, J., Henry, J., & Villanova, M. (1964). État des travaux de cartographie géologique réalisés par la Société Nationale des Pétroles d'Aquitaine (SNPA) dans les Pyrénées occidentales. *Compte Rendu. Sommaire des Séances. Société Géologique de France*, *7*, 241–246.

Serrano, O., Delmas, J., Hanot, F., Vially, R., Herbin, J.-P., Houel, P., & Tourlière, B. (2006). Le bassin d'Aquitaine: valorisation des données sismiques, cartographie structurale et potentiel pétrolier. Bureau de Recherche Géologique et minière.

Souquet, P. (1967). Le Crétacé supérieur Sud-Pyrénéen, en Catalogne, Aragon et Navarre. E. Privat.

Souquet, P., Debroas, E.-J., Boirie, J.-M., Pons, P., Fixari, G., Roux, J.-C., et al. (1985). Le groupe du Flysch noir (albo-cénomanien) dans les Pyrénées. *Bull Cent Rech Exlpo-Prod Elf-Aquitaine Pau*, *9*, 183–252.

Souquet, P., Peybènes, B., Bilotte, M., & Debroas, E.-J. (1977). La chaîne alpine des Pyrénées. *Géologie Alpine*, *53*, 193–216.

Stampfli, G., Mosar, J., Marquer, D., Marchant, R., Baudin, T., & Borel, G. (1998). Subduction and obduction processes in the Swiss Alps. *Tectonophysics*, *296*(1-2), 159–204. https://doi.org/10.1016/S0040-1951(98)00142-5

Teixell, A. (1993). Coupe géologique du massif d'Igountze: implications sur l'évolution structurale de la bordure sud de la zone nord-pyrénéenne occidentale. *Comptes rendus de l'Académie des sciences. Série 2, Mécanique, Physique, Chimie, Sciences de l'univers, Sciences de la Terre*, *316*, 1789–1796.

Teixell, A. (1996). The Anso transect of the southern Pyrenees: Basement and cover thrust geometries. *Journal of the Geological Society*, *153*(2), 301–310. https://doi.org/10.1144/gsjgs.153.2.0301

Teixell, A. (1998). Crustal structure and orogenic material budget in the west central Pyrenees. *Tectonics*, *17*(3), 395–406. https://doi.org/10.1029/98TC00561

Teixell, A., Labaume, P., & Lagabrielle, Y. (2016). The crustal evolution of the west-central Pyrenees revisited: Inferences from a new kinematic scenario. *Comptes Rendus Geoscience*, *348*, 257–267. https://doi.org/10.1016/j.crte.2015.10.010

Ternois, S., Odlum, M., Ford, M., Pik, R., Stockli, D., Tibari, B., et al. (2019). Thermochronological evidence of early orogenesis, eastern Pyrenees, France. *Tectonics*, *38*, 1308–1336. https://doi.org/10.1029/2018TC005254

Thiébaut, J., Debeaux, M., Debroas, E. J., & Souquet, P. (1979). Découverte de roches d'affinités teschenitiques dans les marbres mésozoïques de Saint-Béat (Haute-Garonne). *Comptes Rendus. Académie des Sciences*, *288*, 1695–1697.

Thiébaut, J., Durand-Wackenheim, C., Debeaux, M., & Souquet, P. (1992). Métamorphisme des évaporites triasiques du versant nord des Pyrénées centrales et Occidentales. *Bulletin de la Société d'histoire Naturelle de Toulouse*, *128*, 77–84.

Tugend, J., Manatschal, G., & Kusznir, N. J. (2015). Spatial and temporal evolution of hyperextended rift systems: Implication for the nature, kinematics, and timing of the Iberian-European plate boundary. *Geology*, *43*, 15–18. https://doi.org/10.1130/G36072.1

Turcotte, D. L., & Schubert, G. (2002). *Geodynamics* (2nd ed., p. 456). London: Cambridge University Press.

Unternehr, P., Peron-Pinvidic, G., Manatschal, G., & Sutra, E. (2010). Hyper-extended crust in the South Atlantic: In search of a model. *Petroleum Geoscience*, *16*(3), 207–215. https://doi.org/10.1144/1354-079309-904

Vacherat, A., Mouthereau, F., Pik, R., Bernet, M., Gautheron, C., Masini, E., et al. (2014). Thermal imprint of rift-related processes in orogens as recorded in the Pyrenees. *Earth and Planetary Science Letters*, *408*, 296–306. https://doi.org/10.1016/j.epsl.2014.10.014

Vacherat, A., Mouthereau, F., Pik, R., Huyghe, D., Paquette, J.-L., Christophoul, F., et al. (2017). Rift-to-collision sediment routing in the Pyrenees: A synthesis from sedimentological, geochronological and kinematic constraints. *Earth-Science Reviews*, *172*, 43–74. https://doi.org/10.1016/j.earscirev.2017.07.004

Vauchez, A., Clerc, C., Bestani, L., Lagabrielle, Y., Chauvet, A., Lahfid, A., & Mainprice, D. (2013). Preorogenic exhumation of the North Pyrenean Agly massif (Eastern Pyrenees-France). *Tectonics*, *32*, 95–106. https://doi.org/10.1002/tect.20015

Vergés, J., Fernández, M., & Martinez, A. (2002). The Pyrenean orogen: Pre-, syn-, and postcollisional evolution. *Journal of the Virtual Explorer*, *08*, 55–74. https://doi.org/10.3809/jvirtex.2002.00058

Vergés, J., Millán, H., Roca, E., Muñoz, J. A., Marzo, M., Cirés, J., et al. (1995). Eastern Pyrenees and related foreland basins: Pre-, syn- and post-collisional crustal-scale cross-sections. *Marine and Petroleum Geology*, Integrated Basin Studies, *12*(8), 903–915. https://doi.org/10.1016/0264-8172(95)98854-X

Verschure, R. H., Hebeda, E. H., Boelrijk, N., Priem, H. N. A., & Ave Lallemant, H. G. (1967). K-Ar age of hornblende from a hornblendite vein in the Alpine-type ultramafic mass of the Etang de Lers (Ariege), French Pyrenees. *Leidse Geologische Mededelingen*, *42*, 59–59.

Vielzeuf, D., & Kornprobst, J. (1984). Crustal splitting and the emplacement of Pyrenean lherzolites and granulites. *Earth and Planetary Science Letters*, *67*(1), 87–96. https://doi.org/10.1016/0012-821X(84)90041-4

Wang, Y., Chevrot, S., Monteiller, V., Komatitsch, D., Mouthereau, F., Manatschal, G., et al. (2016). The deep roots of the western Pyrenees revealed by full waveform inversion of teleseismic *P* waves. *Geology*, *44*, 475–478. https://doi.org/10.1130/G37812.1

Wehr, H., Chevrot, S., Courrioux, G., & Guillen, A. (2018). A three-dimensional model of the Pyrenees and their foreland basins from geological and gravimetric data. *Tectonophysics*, *734–735*, 16–32. https://dx.doi.org/10.1016/j.tecto.2018.03.017

Weigel, W., Flüh, E. R., Miller, H., Butzke, A., Dehghani, G. A., Gebhardt, V., et al. (1995). Investigations of the East Greenland continental margin between 70 and 72 N by deep seismic sounding and gravity studies. *Marine Geophysical Researches*, *17*(2), 167–199. https://doi.org/10.1007/BF01203425

Wopenka, B., & Pasteris, J. D. (1993). Structural characterization of kerogens to granulite facies graphite: applicability of Raman microprobe spectroscopy. *American Mineralogist*, *78*, 533–557.

Yui, T. F., Huang, E., & Xu, J. (1996). Raman spectrum of carbonaceous material: A possible metamorphic grade indicator for low-grade metamorphic rocks. *Journal of Metamorphic Geology*, *14*(2), 115–124. https://doi.org/10.1046/j.1525-1314.1996.05792.x

Zhou, Q., Xiao, X., Pan, L., & Tian, H. (2014). The relationship between micro-Raman spectral parameters and reflectance of solid bitumen. *International Journal of Coal Geology*, *121*, 19–25. https://doi.org/10.1016/j.coal.2013.10.013

References From the Supporting Information

Förster, A., Merriam, D. F., & Davis, J. C. (1997). Spatial analysis of temperature (BHT/DST) data and consequences for heat-flow determination in sedimentary basins. *Geologische Rundschau*, *86*(2), 252–261. https://doi.org/10.1007/s005310050138

Garibaldi, C., Guillou-Frottier, L., Lardeaux, J. M., Bonté, D., Lopez, S., Bouchot, V., & Ledru, P. (2010). Thermal anomalies and geological structures in the Provence basin: Implications for hydrothermal circulations at depth. *Bulletin de la Societe Geologique de France*, *181*(4), 363–376. https://doi.org/10.2113/gssgfbull.181.4.363

Goutorbe, B., Lucazeau, F., & Bonneville, A. (2007). Comparison of several BHT correction methods: A case study on an Australian data set. *Geophysical Journal International*, *170*(2), 913–922. https://doi.org/10.1111/j.1365-246X.2007.03403.x

Jaupart, C., & Mareschal, J.-C. (2007). Heat flow and thermal structure of the lithosphere. In *Treatise on Geophysics, G. Schubert* (pp. 217–251). Elsevier.

Rabinowicz, M., Boulègue, J., & Genthon, P. (1998). Two- and three-dimensional modeling of hydrothermal convection in the sedimented Middle Valley segment, Juan de Fuca Ridge. *Journal of Geophysical Research*, *103*(B10), 24,045–24,065. https://doi.org/10.1029/98JB01484